Natural Resources Canada | Ressources naturelles Canada

GEOLOGICAL SURVEY OF CANADA
OPEN FILE 8954

# Use of CT-scan images to build geomaterial 3D pore network representation in preparation for numerical simulations of fluid flow and heat transfer, Quebec

A. Hammouti, S. Larmagnat, C. Rivard, and D. Pham Van Bang

2023

Canada

**GEOLOGICAL SURVEY OF CANADA**
**OPEN FILE 8954**

# Use of CT-scan images to build geomaterial 3D pore network representation in preparation for numerical simulations of fluid flow and heat transfer, Quebec

**A. Hammouti[1], S. Larmagnat[2], C. Rivard[2], and D. Pham Van Bang[1]**

[1]Institut National de la Recherche Scientifique - Centre Eau Terre Environnement, 490, rue de la Couronne, Québec, Quebec
[2]Geological Survey of Canada, 490, rue de la Couronne, Québec, Quebec

## 2023



Permanent link: https://doi.org/10.4095/331502

This publication is available for free download through GEOSCAN (https://geoscan.nrcan.gc.ca/).

**Recommended citation**
Hammouti, A., Larmagnat, S., Rivard, C., and Pham Van Bang, D., 2023. Use of CT-scan images to build geomaterial 3D pore network representation in preparation for numerical simulations of fluid flow and heat transfer, Quebec; Geological Survey of Canada, Open File 8954, 49 p. https://doi.org/10.4095/331502

Publications in this series have not been edited; they are released as submitted by the author.

ISSN 2816-7155
ISBN 978-0-660-47745-9
Catalogue No. M183-2/8954E-PDF

# Table of Contents

Table of Contents ..... i

List of Figures ..... iii

List of Tables ..... ix

Abstract ..... 1

1. Introduction ..... 2

2. Definitions and Theory ..... 4

2.1 Definitions ..... 4

2.2 Theory ..... 6

3. Methodology ..... 9

3.1 Selection of materials ..... 9

3.1.1 Glass bead models ..... 9

3.1.2 Reference rock samples ..... 9

3.2 Experimental measurements ..... 10

3.2.1 Medical CT (med-CT) imaging ..... 10

3.2.2 Gas porosity and permeability measurements ..... 12

3.3 Numerical modeling and prior validation ..... 12

3.3.1 Prior validation using a glass bead assembly ..... 12

3.3.2 Selection of the scale ..... 13

3.3.3 Mesoscopic modeling using glass beads and rock samples ..... 13

4. Description of previous work on pore-scale modeling ..... 14

4.1 Use of a glass-bead model ..... 14

4.1.1. Image acquisition and segmentation ..... 14

4.1.2. Meshing the pore space ..... 15

4.1.3. Coupling of hydrodynamic flow with heat transfer ..... 17

4.2. Use of a concrete sample ..... 19

5. Estimation of effective porosity and preparation for flow modeling work at the meso-scale ..... 21

5.1. Phase identification and porosity estimation ..... 21

5.2. Effective porosity ..... 21

5.2.1. Case study of a near-ideal porous medium: the glass bead assembly ..... 21

5.2.2. Boise sandstone core sample ..... 25

5.2.3. Berea sandstone core sample ..... 30

5.2.4. Indiana limestone core sample ..... 33

5.3 Influence of the core sample diameter on the effective porosity evaluation ..... 37

5.4 Future work ..... 41

5.4.1. Projection of morphologies on an unstructured mesh ..... 41

5.4.2. Technical challenges ..... 43

5.4.3 Perspectives: Toward a CFD Coupling ..... 44

6. Conclusion and perspectives ..... 46

7. References ..... 47

# List of Figures

Figure 1: Summary of the Tomoporoflow study workflow. Part I of the study is the subject of the present report and focuses on how the geometry of the pore network can be realistically extracted (porosity type, size of pores, etc.). Note: DEM refers to Discrete Element Method. ..... 3

Figure 2: Illustration of the different types of pores in a rock and formulas used for their calculation, adapted from Yokoyama and Takeuchi (2009). ..... 4

Figure 3: Illustration of the three scales described in this study: micro, meso and macro ..... 7

Figure 4: (a) Decomposition of the domain into layers of thickness dz. (b) Example of raw data from a horizontal slice of a micro X-ray CTscan of a concrete sample (Stamati et al., 2018a), where the color scale corresponds to a positive linear function of the Hounsfield Unit (HU), i.e. a quantitative scale for describing radiodensity. ..... 11

Figure 5: Illustration showing the workflow for image processing of glass-bead assembly (Oukaili, 2019)..... 15

Figure 6: Illustration of the different stages of object segmentation using the Watershed algorithm in MATLAB (from Oukaili, 2019)..... 15

Figure 7: Illustrations of the 269 glass-bead assembly showing three different stages of the workflow (Hammouti et al., in preparation): (a) A TIFF-file after med-CT scanning (b) An STL-file after the 1-2% reduction of each glass bead (c) DEM (data exchange mode) file showing an area inside the fluid domain generated after meshing..... 16

Figure 8: Cross-section of the mesh of a sample composed of glass beads scanned with the med CT-scan (Hammouti et al., in preparation). The mesh was generated using the Salome software. This illustrates how the erosion algorithm helps the mesh generator by slightly increasing the space between the particles (here beads), ensuring that at least one voxel separates each particle. Note: The beads have all the same diameter (16 mm ± 3%), but since this cross-section shows a xy plane, the beads are not all cut in their center..... 17

Figure 9: (a) Configuration of an assembly of spherical particles generated numerically using a DEM (Discrete Element Method) (b) Configuration of a scanned assembly made of 269 glass beads (medical CT-scan images). Taken from Hammouti et al. (in preparation). ..... 18

Figure 10: Results of numerical simulations for flow through a cylinder containing 110 spherical particles, where velocity (**u**) and temperature (T) fields are imposed through boundary conditions at

the bottom (u=0.2 and T=1) and at the top (du/dz=0, dT/dz=0 and p=0). All fields (velocity and pressure) are dimensionless. (a) Velocity and pressure profiles are provided along the z-axis for x= 2.5 cm and y=3.5 cm). (b) Temperature profile along the z-axis also for x= 2.5 cm and y=3.5 cm. Figures are adapted from Hammouti et al. (in preparation) and Oukaili (2019). ..... 19

Figure 11: Images of a scanned concrete sample, generated from a micro-CT dataset made available by Stamati et al. (2018a). (a) 3D trinary image - blue: macro- and micro-pores, light grey: aggregates and the rest is occupied by the mortar matrix. (b) Horizontal slice at the middle of the sample showing the identified phases. Phase 0 (white): outside the media, phase 1: mortar, phase 2: pores, phase 3 (black): aggregates. X-ray image dimensions are [nx,ny,nz]=[250,250,400] and resolution dx=dy=dz=0.055 mm. ..... 20

Figure 12: (a) Longitudinal view (x-z plane) of the concrete sample from Stamati (2018a). b) Total porosity profile averaged for each x-y plane plotted along the z-axis. The average total porosity is 2.76%. ..... 20

Figure 13: Glass-bead assembly - (a) STL-file of the 269 glass-bead assembly, with dimensions [nx,ny,nz]=[512,512,771] and resolutions of dx=dy=0.15mm and dz=0.4mm (obtained with the medical CT-Scan). (b) Horizontal slice showing the identified phases (mid sample) – phase 0: outside the media, phase 1: interconnected pore space, phase 2: glass beads (Hammouti et al., in preparation). ..... 22

Figure 14: Glass-bead assembly - (a) Lateral (x-z) and radial (x-y) planes of the glass bead sample showing the pore space, taken from Hammouti et al. (in preparation) (b) Porosity profile of this sample, after binarization and removal of a top and bottom layer equivalent to 3 times the average sphere diameter (red dotted lines). ..... 22

Figure 15: Glass-bead assembly - Representation of the pore network of the 269 glass-bead assembly along slice 385 for the x-y axis and slice 256 for the x-z axis. a) raw data, b) after binarization using Otsu's algorithm (Otsu, 1979) and (c) after segmentation using the ITK Watershed algorithm to separate the glass beads. ..... 23

Figure 16: Glass-bead assembly - Statistical distribution of the glass bead size within the sample obtained using the ITK Watershed algorithm. A total of 269 glass beads were identified. The minimum glass bead volume is 196 611 voxels (corresponding to 1769.5 $mm^3$) and the maximum glass bead volume is 260 936 voxels (2348.4 $mm^3$). 1 voxel = dx*dy*dz. Of note, a maximum tolerance of $\varepsilon tol = 3\%$ on the diameter leads to a maximum of $\varepsilon tol3 = 27\%$ on the volume. ..... 24

Figure 17: Glass-bead assembly - Mean (MSD) and axial (ASD) square displacement for the different axes (0: z-axis 1: x-axis 2: y-axis) versus time. The plain lines represent the actual results and the dotted lines are the linear regressions for which the slope defines the tortuosity (Tau). The higher the square displacement over time, the lower the tortuosity (since the fluid takes a shorter path to pass through the sample). ..... 25

Figure 18: Boise sample (BO-K15B) with dimensions [nx,ny,nz]=[512,512,78] and resolution dx=dy=0.1mm and dz=0.6 mm (a) 3D view of the connected porosity network estimated using med-CT images from saturated and dry states, from Larmagnat, et al. (2019). The grey scale indicates the amount of water replacing air in the sample: from 0% (black, i.e. a voxel completely occupied by the geomaterial) to 100% (white, i.e. a voxel completely occupied by a pore). (b) 3D view illustrating binarized med-CT images using Spam and (c) transversal slice through the binarized dataset showing the different phases (in the middle of the sample) – phase 0 (white): outside the media, phase 1 (grey): pores, phase 2 (black): matrix. Note: When presenting binarized results, Spam uses a continuous scale, although only three values (0, 1 and 2) are actually used. ..... 26

Figure 19: Boise sandstone sample - Porosity profiles along the sample (z in mm). Although the values are more variable in the case of the binarized dataset, average values are very similar for the subtracted (30.8%) and binarized datasets (30.2%). ..... 27

Figure 20: Boise sandstone sample - Representation of the pore network along slice 41 for the x-y axis and slice 256 for the x-z axis. a) Subtracted data: The blue scale indicates the amount of water (from 0% (white, i.e. a voxel with no pore) to 100% (white, i.e. a voxel completely occupied by a pore), b) after binarization (dark blue: pores, white: matrix) using Otsu's method (Otsu, 1979) and (c) after segmentation using the ITK Watershed algorithm to separate macropores. ..... 28

Figure 21: Boise sandstone sample - Statistical distribution of the (macro) pore size of the Boise sandstone using the ITK Watershed algorithm: a) semi-log plot presenting the entire population b) linear plot best showing the majority of the population. ..... 29

Figure 22: Boise sandstone sample - Mean (MSD) and axial (ASD) square displacement (0: z-axis 1: x-axis 2: y-axis) versus time for the Boise sandstone sample. The plain lines represent the actual results and the dotted lines are the linear regressions for which the slope defines the tortuosity (Tau). ..... 30

Figure 23: Berea sample (BE-K15B) with dimensions [nx,ny,nz]=[512,512,78] and resolution dx=dy=0.1mm and dz=0.6mm. (a) 3D view of the connected porosity network estimated using med-CT images from saturated and dry states, from Larmagnat, et al. (2019). The grey scale indicates the amount of water replacing air in the sample: from 0% (black, i.e. a voxel completely occupied by the

geomaterial) to 100% (white, i.e. a voxel completely occupied by a pore). (b) 3D view illustrating binarized med-CT images using Spam and (c) transversal slice through the binarized dataset showing the different phases (in the middle of the sample) – phase 0 (white): outside the media, phase 1 (grey): pores, phase 2 (black): matrix. Note: When presenting binarized results, Spam uses a continuous scale, although only three values (0, 1 and 2) are actually used. ..... 30

Figure 24: Berea sandstone sample - Effective porosity profile of the Berea sample BE-K15B. The average value for the subtracted dataset is 19.3% and for the binarized dataset is 17.3%. ..... 31

Figure 25: Berea sandstone sample - Representation of the effective pore network along slice 41 for the x-y axis and slice 256 for the x-z axis. a) Subtracted data: Blue scale indicates the amount of water (from 0% (white, i.e. a voxel with no pore) to 100% (white, i.e. a voxel completely occupied by a pore), b) after binarization (blue phase : pores, white phase : matrix) using Otsu's method (Otsu, 1979) and (c) after segmentation using the ITK Watershed algorithm to separate macropores. ..... 32

Figure 26: Berea sandstone sample - Statistical distribution of the (macro) pore size of the Berea sandstone using the ITK Watershed algorithm: a) linear plot best showing the majority of the population b) semi-log plot presenting the entire population. ..... 33

Figure 27: Berea sandstone sample - Mean (MSD) and axial (ASD) square displacement (0: z-axis 1: x-axis 2: y-axis) versus time for the Berea sandstone sample. The plain lines represent the actual results and the dotted lines are the linear regressions for which the slope defines the tortuosity (Tau). ..... 33

Figure 28: Indiana limestone sample (IN-C15A) with dimensions [nx,ny,nz]=[512,512,159] and resolution dx=dy=0.1mm and dz=0.6mm. (a) 3D view of the effective porosity dataset estimated using med-CT images from saturated and dry states, from Larmagnat, et al. (2019). The grey scale indicates the amount of water replacing the air space in the sample: from 0% (black, i.e. a voxel completely occupied by the geomaterial) to 100% (white, i.e. a voxel completely occupied by a pore). (b) 3D view illustrating binarized med-CT using Spam and (c) transversal slice through the binarized dataset showing the different phases (in the middle of the sample) – phase 0 (white): outside the media, phase 1 (grey): pores, phase 2 (black): matrix. ..... 34

Figure 29: Indiana limestone sample - Effective porosity profile for the Indiana sample IN-C15A. The average value for the subtracted data is 14.7% and for the binarized data is 13.5%. ..... 34

Figure 30: Indiana limestone sample - Representation of the effective pore network along slice 79 for the x-y axis and slice 256 for the x-z axis. a) Subtracted data: The blue scale indicates the amount of water (from 0% (white, i.e. a voxel with no pore) to 100% (white, i.e. a voxel completely occupied by

a pore), b) after binarization (blue phase : pores, white phase : matrix) using Otsu's method (Otsu, 1979) and (c) after segmentation using the ITK Watershed algorithm to separate macropores..... 35

Figure 31: Indiana limestone sample - Statistical distribution of the (macro) pore size of the Indiana limestone sample using the ITK Watershed algorithm: a) linear plot best showing the majority of the population b) semi-log plot presenting the entire population. ..... 36

Figure 32: Indiana limestone sample - Mean (MSD) and axial (ASD) square displacement (0: z-axis 1: x-axis 2: y-axis) versus time for the Indiana limestone sample. The plain lines represent the actual results and the dotted lines are the linear regressions for which the slope define the tortuosity (Tau). ..... 37

Figure 33: Numerical assessment of the effective porosity according to three diameters within the Boise sandstone sample (D= 32.42 mm (blue line), 24.30 mm (orange line) and 16.20 mm (green line)): (a) cross-section from the binarized dataset and (c) cross-section from the subtracted dataset showing the different diameters with colors (blue, green and orange). Effective porosity profiles of theses samples: (b) for the binarized datasets and (d) for the subtracted datasets. The average ($\varepsilon_m$) and standard deviation ($\sigma$) effective porosity values are given for each sampling diameter. ..... 38

Figure 34: Numerical assessment of the effective porosity according to three different diameters with the Berea sandstone sample (D= 31.82 mm (blue line), 24.88 mm (orange line) and 15.92 mm (green line)): (a) cross-section from the binarized dataset and (c) cross-section from the subtracted dataset showing the different diameters with colors (blue, green and orange). Effective porosity profiles of theses samples: (b) for the binarized datasets and (d) for the subtracted datasets. The average ($\varepsilon_m$) and standard deviation ($\sigma$) effective porosity values are given for each sampling diameter. ..... 40

Figure 35: Numerical assessment of the effective porosity according to three different diameters with the Indiana limestone sample (D= 33.00 mm (blue line), 24.75 mm (orange line) and 16.50 mm (green line)): (a) cross-section from the binarized dataset and (c) cross-section from the subtracted dataset showing the different diameters with colors (blue, green and orange). Effective porosity profiles of theses samples: (b) for the binarized datasets and (d) for the subtracted datasets. The average ($\varepsilon_m$) and standard deviation ($\sigma$) effective porosity values are given for each sampling diameter. ..... 41

Figure 36: Example of a morphology-independant mesh method for a concrete sample: (a) segmented 3D image (b) a void unstructured mesh (c) the result of this projection: the projected mesh. Adapted from (Stamati et al., 2018b)..... 42

Figure 37: Example of a projection for a concrete sample: (a) Illustration of the projection of each inclusion type phase. Color code: Material 1 (dark blue): mortar, Material 2 (light blue): aggregates,

material 3 (green): interface mortar/aggregates, Material 4 (orange): pores and Material 5 (red) interface mortar/pores. (b) Illustration of pores (Material 4 & 5) (c) representation of the normals of pore surfaces. ..... 42

Figure 38: (a) Example of a 3D view illustrating connected porosity matrices of a Silurian core sample CSI-11 from [Larmagnat et al., 2019]. The grey scale indicates porosity: from 0% (black) to 100% (white). (b) a 3D view of a binarized pore network (c) Effective porosity profile of this sample. The average porosity value for this core plug for the non-binarized data is 4.9% and for the binarized data is 4.4%. Note: over the first 50 mm of the sample, the porosity is lower than in the rest of the sample (around 4.4-4.9%) and includes micro-pores, so the binarized dataset underestimates their value... 44

Figure 39: Illustration of the multi-scale approach to be used in support to geothermal energy modeling..... 45

# List of Tables

Table 1 – Permeability and porosity ranges for different types of unconsolidated sediments and rocks (adapted from Jasim et al., 2018 and references therein)..... 6

Table 2: Size of the reference core samples used in this study, along with their estimated gas porosity..... 10

Table 3 : Scanning parameters used for both the glass-bead model and the two reference rock samples. kV stands for kilovoltage, mAs for milliampere-second and F.O.V stands for field of view.. 10

# Abstract

Non-intrusive techniques such as medical CT-Scan or micro-CT allow the definition of 3D connected pore networks in porous materials, such as sedimentary rocks or concrete. The definition of these networks is a key step towards the evaluation of fluid flow and heat transfer in energy resource (e.g., hydrocarbon and geothermal reservoirs) and $CO_2$ sequestration research projects. As material heterogeneities play a role at all scales (from micro- to project-scale), numerical models represent a powerful tool for bridging the gap between small-scale measurements provided by X-ray imaging techniques and larger-scale transport properties.

This study uses pre-existing medical CT-scan datasets of reference material, namely glass beads and conventional reservoir rocks (Berea sandstone, Boise sandstone, Indiana limestone) to extract the 3D geometry of connected pores using an open-source software (Spam). Pore networks from rock samples were generated from dry and then saturated samples. Binarized datasets were produced for these materials (generated by a thresholding technique) to obtain pore size distribution and tortuosity, as well as preferential paths for fluid flow. Average porosities were also calculated for comparison with those obtained by conventional commercial laboratory techniques. The results obtained show that this approach works well for medium and coarse-grained materials that do not contain a large percentage of fine particles. However, this approach does not allow representative networks to be obtained for fine-grained rocks, due to the fact that small pores (or pore throats) cannot be taken into account in the datasets obtained from the medical CT-Scan. A next step, using datasets produced from a micro-CT scan, is planned in order to be able to generate representative networks in this type of material as well.

*Key words* : CT-scan, porous media, 3D pore networks, geomaterials, CFD

# 1. Introduction

The current study is part of a larger project aiming at characterizing the geothermal energy potential of the Bécancour area in the St. Lawrence Lowlands of southern Québec, funded by the Geoscience for New Energy Supply (GNES) program of the Geological Survey of Canada (GSC). Geothermal heat production at intermediate depths (1-2 km) for diverse domestic and industrial purposes is currently not part of the Canadian low-carbon energy portfolio. Understanding fluid circulation and heat transfer is critical to the successful development of such projects. Characterization of sub-surface sedimentary units provides the fundamental information that will help evaluate the technical and economic feasibility of intermediate to deep geothermal heat generation projects. An accurate definition of porosity networks, and thus indirectly of permeability, at the submeter-scale is generally lacking, while this fundamental aspect controls the ability of rocks to store and circulate fluid and therefore to build better models of fluid flow in the subsurface. Without detailed information on hydrogeological properties in 3D and at different scales (from core samples to the entire geothermal reservoir), current conventional approaches to evaluate fluid circulation, and ultimately help maximize heat extraction or $CO_2$ sequestration, can lead to ambiguous or unrealistic results.

Our long-term goal is to provide a critical fine-scale understanding of the physical properties of rocks to model fluid flow from the pore scale to the local scale (e.g. around a well) for future use in real-world geothermal, $CO_2$ sequestration or oil and gas projects. To do so, the present study builds on preexisting numerical work (Hammouti et al., in preparation; Larmagnat et al., 2019; Oukaili, 2019) and on the application of non-destructive techniques such as X-ray imaging technique and more specifically computed tomography (CT) to document the fundamental properties of porous material (e.g., sedimentary rocks and concrete), so as to test computational techniques aiming at numerically generating connected pore networks for future fluid flow and heat transport simulations. The key challenge is to bridge the gap between the small-scale measurements provided by medical CT-Scan (hereafter referred to as “med-CT”) or micro-CT-scan imaging techniques and macro-scale physical properties to model fluid flow, and eventually heat transport, in porous geomaterials. In the present report, we explore different techniques to import meso and macrostructures from images obtained by preexisting med-CT measurements into a Computational Fluid Dynamic (CFD) code. Two types of reference materials are considered, corresponding to a progressive degree of complexity: (1) perfectly rounded and monosized beads to develop the methodology; then (2) reference reservoir rocks from the oil and gas industry (relatively homogeneous and permeable) as an initial step towards core samples from actual case studies. The developed approach is entirely based on open-source codes.

The main objective of this first part of the study is to numerically generate 3D interconnected pore networks (i.e., neglecting isolated pores and dead-ends which do not participate in fluid flow). To this end, various approaches were investigated to efficiently extract the 3D pore space network from med-CT images of geomaterials. Only the one that was selected, as considered the most relevant, is presented here. The approach used for the numerical simulations for fluid flow is also discussed, based on previous work with the glass bead model. The second part of this study (in preparation, thus not presented here) will present the results of the numerical fluid flow simulations performed using pore space meshes extracted from CT images of different geomaterials. Heat transfer and $CO_2$ injection will eventually be introduced as a second degree of complexity. Depending on the availability of data (physical model experiments using novel equipment are planned or, in the worst-case scenario, existing reference cases), the newly developed methodology will be applied for validation and/or prediction. The approach for the Tomoporoflow study, including both phase I and II, as well as previous work (i.e., glass bead model), is summarized in Figure 1.

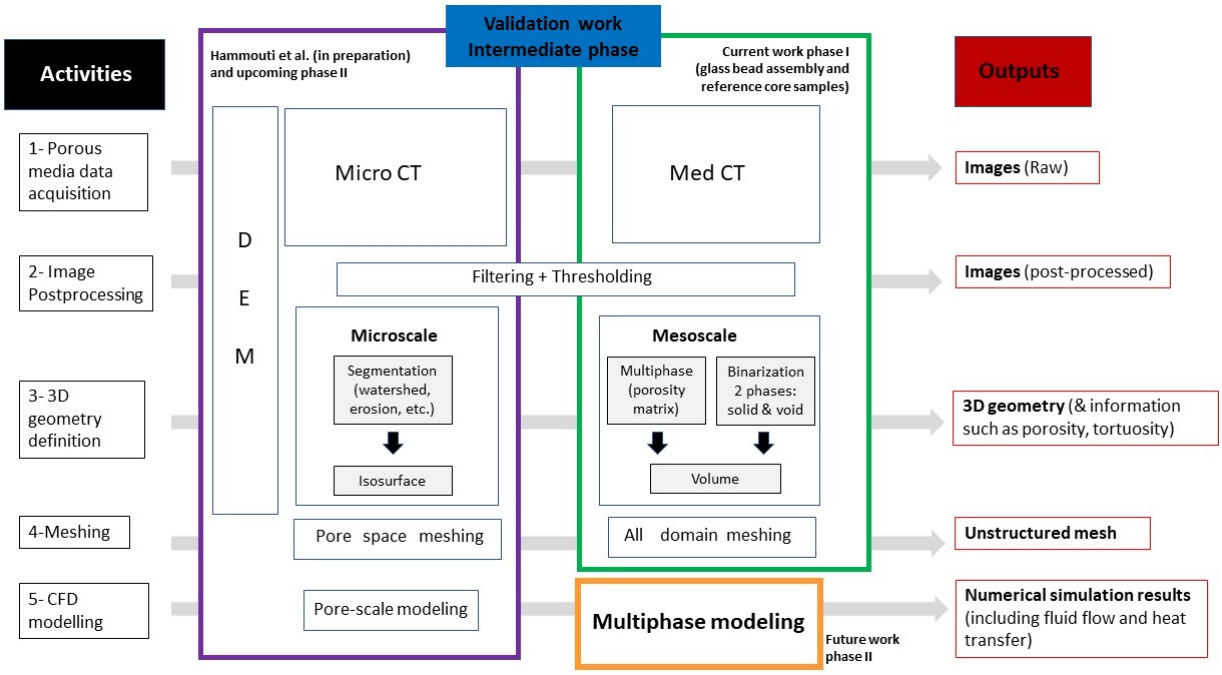


Figure 1: Summary of the Tomoporoflow study workflow. Part I of the study is the subject of the present report and focuses on how the geometry of the pore network can be realistically extracted (porosity type, size of pores, etc.). Note: DEM refers to Discrete Element Method and CFD stands for Computational Fluid Dynamic.

A potential future application of this work, once a sufficient number of samples have been processed, would be the development of a database containing different measurements (porosity, permeability, thermal conductivity, and heat capacity) for various lithologies and their mapping, which could provide

a rapid preliminary assessment of the potential for $CO_2$ storage or heat production of new rock samples or a given area through an AI or machine learning strategy.

# 2. Definitions and Theory

## 2.1 Definitions

Three definitions for the different types of porosity (ε) are provided here, based on several reference documents (API, 1998; Cantrell and Hagerty, 1999; Choquette and Pray, 1970; Lucia et al., 2003; Pittman, 1971; Ramsey, 2019). The total porosity is defined as the fraction of the bulk rock value Vb that is not occupied by solid matter (i.e. rock phase in our case, Vg). It thus represents the total void space, which includes isolated pores and dead-ends, and even the space occupied by clay-bound water (Figure 2). This corresponds to the porosity measured by conventional core analysis techniques that involve disaggregating the sample (API, 1998). It also corresponds to the porosity inferred from many borehole logging measurements, including density, neutron porosity and nuclear magnetic resonance logs (Schlumberger, 1989).

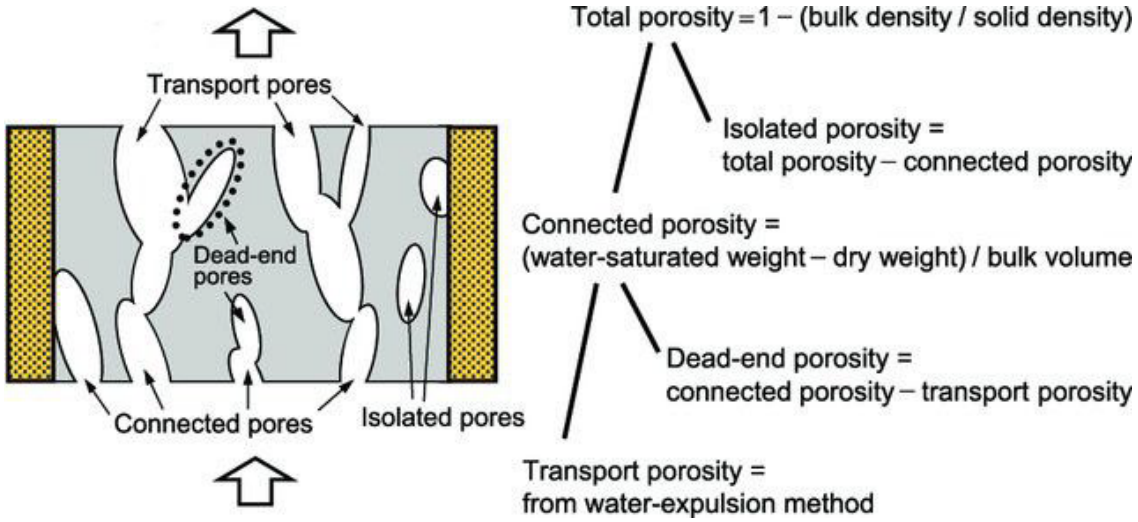


Figure 2: Illustration of the different types of pores in a rock and formulas used for their calculation, adapted from Yokoyama and Takeuchi (2009). Note: these formulas consider fresh water (with a density of 1 g/ml or 1 g/cm3).

Microporosity is commonly considered to be that part of the pore space with a characteristic size being less than 1 or 2 microns, but definitions differ between authors. It is also sometimes defined as the porosity that cannot be observed at magnifications below 50x (Cantrell and Hagerty, 1999; Pittman, 1971).

Pores can be classified into three categories. Distinguishing between them is crucial to correctly simulate fluid flow and heat transfer:

- Isolated pores: they do not communicate with the outside environment.
- Connected pores: they form a limited connected space in the porous medium and participate in the transport of fluid through the material, but can contain dead-end pores.
- Dead-end pores: they are interconnected on one side only and are accessible to an external fluid, but they do not participate in its transport.

Pore volume and total porosity can be calculated using the equations 1 and 2:

$$Vpores = Vb - Vg \tag{1}$$

where Vg is the volume of grains

$$Total\ porosity\ \varepsilon = \frac{Pore\ Volume}{Total\ rock\ Volume} = \frac{Vb - Vg}{Vb} = \frac{Vpores}{Vb} \tag{2}$$

Effective porosity is defined as the fraction of the interconnected non-solid volume allowing flow through the rock. For the purpose of this work, we consider that the effective porosity is close to the connected porosity, which itself should be representative of the transport porosity in many materials. It is therefore always lower than the total porosity, to varying degrees. Effective porosity is commonly measured in a laboratory using gas or liquid flowing through a known rock volume measured using caliper (API, 1998). In the oil and gas industry, core plugs are typically 1 or 1.5 inches in diameter.

The porosity of natural materials varies over a wide range (Table 1, as geological formations are composed of very different materials (from fine to coarse). Their porosity can also change over time due to the fact that formations can have a very complex history, involving for example consolidation, cementation, and fracturing. Porosity is commonly subdivided into primary and secondary porosity, where primary porosity is considered to result from the original depositional structure, whereas secondary porosity results from diagenesis (and thus includes fractures).

The permeability of a material, (i.e., the ability to transmit fluids) is strongly related to its porosity and more specifically to the effective (interconnected or transport) porosity, as well as to the tortuosity of the configuration and thus to the global heterogeneity of the material. The term tortuosity was first introduced by Carman (1956) and is usually defined as the measure of the complexity of fluid pathways in porous media, which includes their sinuosity and interconnectivity. However, multiple definitions of tortuosity can be found in the literature (e. g. Fu et al., 2021; Yang et al., 2019) with minor differences,

which mainly depend on the method used to characterize/measure it. There is, to some extent, a correlation between porosity, tortuosity and permeability: as porosity (especially effective porosity) increases, tortuosity decreases (as pores become more connected) and thus permeability increases.

Table 1 – Permeability and porosity ranges for different types of unconsolidated sediments and rocks (adapted from Jasim et al., 2018 and references therein).

| | Permeability ($m^2$) | | Porosity (%) |
|---|---|---|---|
| **Type** | **Min** | **Max** | **Range** |
| ***Unconsolidated sediments*** | | | |
| Gravel | $10^{-10}$ | $10^{-7}$ | 25-40 |
| Clean sand | $10^{-13}$ | $10^{-9}$ | 5-50 |
| Silty sand | $10^{-14}$ | $10^{-10}$ | - |
| Silt, Loess | $10^{-16}$ | $10^{-12}$ | 35-50 |
| Unweathered clay | $10^{-20}$ | $10^{-15}$ | 40-80 |
| ***Rocks*** | | | |
| Shale | $10^{-20}$ | $10^{-16}$ | 0-10 |
| Unfractured metamorphic and igneous | $10^{-20}$ | $10^{-17}$ | 0-5 |
| Sandstone | $10^{-17}$ | $10^{-13}$ | 5-35 |
| Limestone and dolomite | $10^{-16}$ | $10^{-13}$ | 0-20 |
| Fractured igneous and metamorphic | $10^{-15}$ | $10^{-13}$ | 0-10 |
| Permeable basalt | $10^{-14}$ | $10^{-9}$ | 0-25 |
| Karst limestone | $10^{-13}$ | $10^{-9}$ | 5-50 |

Permeability is difficult if not impossible to evaluate theoretically or from formulas (e.g. from grain size analysis) because it depends on many complex factors, including in addition to porosity and tortuosity: the geometrical features of the void space (that include the pore size distribution, the shape and size of the grains, and the roughness of the solid surface), which all play a role in the overall heterogeneity of the material. Due to these factors, it is difficult to obtain a representative value of this parameter even through a laboratory experiment (e.g. using a column by applying a pressure gradient, as in the Darcy's famous experiment on the flow of water through sands) or in the field (e.g using a pumping test), because depending on the sample or site tested, as well as its size, the value can vary considerably.

## 2.2 Theory

Flow through porous materials occurs at all scales, from nanoscale structures to the macro scale (e.g. around a well) to the regional (watershed) or supra-regional (basin) scale and have been the subject

of extensive studies (Aharonov et al., 1997; Chapman, 1987; McDowell‐Boyer et al., 1986; Neglia, 1979; Noiriel and Soulaine, 2021; Steefel et al., 2015). Darcy's law is valid in many cases, however in some situations, the relation between the pressure gradient and velocity field is no longer linear and Darcy's law does not provide accurate results (Ergun, 1952; Ward, 1964). For instance, Darcy's law has been found to be invalid for high values of Reynolds number and at very low values of hydraulic gradient in some very low-permeability materials, such as clays, as well as at very fine scales. For this study, the notion of porosity was described at three scales: micro, meso and macro, as illustrated in Figure 3.

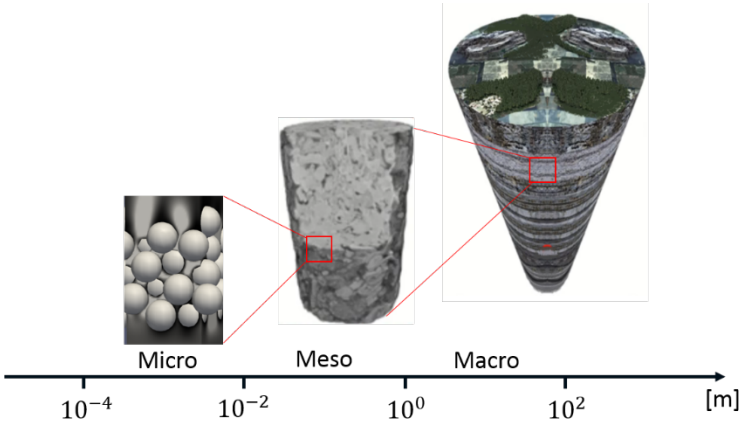


Figure 3: Illustration of the three scales described in this study: micro, meso and macro.

The micro-scale is used to describe what happens at a given point within a fluid (or solid) phase continuum (Bear, 2018). The micro-scale model takes into account the distribution and architecture of the pores, thus modeling the multiphase flow (typically including gas and water) allows the study of the main transport processes by taking into account most of non-Darcian effects such as inertial effects, which become large compare to viscous effects at high Reynolds numbers. For flow at this scale, the model uses the conservation equations for momentum and mass described as:

$$\frac{\partial \rho \boldsymbol{u}}{\partial t} + \nabla \cdot (\rho \boldsymbol{u}\boldsymbol{u}) = \boldsymbol{\nabla} \cdot \boldsymbol{\tau} - \boldsymbol{\nabla} p + \boldsymbol{F} \tag{3}$$

$$\frac{\partial \rho}{\partial t} + \nabla \cdot (\rho \boldsymbol{u}) = \mathbf{0} \tag{4}$$

with $\tau = \mu \left(\nabla \mathbf{u} + (\nabla \boldsymbol{u})^T\right)$

where ρ, μ, $\boldsymbol{u}$, p correspond respectively to the fluid density (kg/m$^3$), dynamic viscosity (Pa.s), velocity (m/s), and pressure (Pa). In this study, we consider the fluid to be incompressible (ρ is constant) and the body force **F** (Pa/m) due only to gravity **g.** Initial and boundary conditions need to be specified

according to the configuration of the studied sample. The description of fluid–solid boundaries for a given porous medium domain at this scale is highly dependent on the resolution of the imaging and the computing power.

At the macroscopic scale (also called Darcy scale), the basic law describing laminar flow in porous materials is Darcy's law (Darcy, 1856), which was first an empirical law, but was later derived theoretically from the Navier–Stokes equation. It describes a linear relationship between the velocity field **u** and the pressure drop $\Delta$p/L:

$$\boldsymbol{u} = -\frac{k}{\mu}\frac{\boldsymbol{\Delta} p}{L} \quad \text{or} \quad = -K\frac{\boldsymbol{d}h}{dl} \text{ in differential form, since K} = \frac{k\rho g}{\mu} \tag{5}$$

with *k* ($m^2$) is the permeability of the porous medium, $\Delta p$ (Pa) the pressure difference between outflow and inflow boundary, *L* (m) the distance between inflow and outflow, *K* is the hydraulic conductivity (m/s) *h* is the hydraulic head (m) and *dh/dl* is the hydraulic gradient. Numerous purely empirical formulæ that relate permeability to various geometric properties of the void space were presented in the literature (e.g., Hagen–Poiseuille law: the steady state solution of the Navier–Stokes equations for a capillary tube). However, Kozeny (1927) was the first to describe a porous medium as a collection of small channels through which a fluid flows. His formula was then improved by Carman and for laminar flow, the equation (still widely used today) of the Kozeny-Carman equation is the following:

$$\frac{\boldsymbol{\Delta} p}{L} = \alpha\frac{(1-\varepsilon)^2\,\Sigma^2}{\varepsilon^3}\,\mu\boldsymbol{u} \tag{6}$$

where $\varepsilon$ is the total porosity of media (volumetric ratio of void space to total space), $\Sigma$ the specific surface area of the solid grains (defined per unit volume of solid matrix), $1/\Sigma$ is often taken equal to $d_{50}$, the geometrical mean grain size obtained from grain-size analysis, $\alpha$ is a coefficient determined empirically, corrected by Carman (Carman, 1937; Carman, 1956).

Later, Burke and Plummer (1928) extended Darcy's law for high Reynolds numbers, considering that the pressure drop across a bed of packed particles can be calculated as an inertia term, inspired by the approach of Kozeny (1927):

$$\frac{\boldsymbol{\Delta} p}{L} = \beta\frac{(1-\varepsilon)\,\Sigma}{\varepsilon^3}\,\rho\boldsymbol{u}^2 \tag{7}$$

where $\beta$ is a coefficient determined by experimental data.

Ergun (1952) combined the Kozeny-Carman and Burke-Plummer equations together, producing a mathematically blended model to predict laminar, transitional, or turbulent flow, which satisfies the linear and nonlinear terms:

$$\frac{\boldsymbol{\Delta p}}{L} = \alpha \frac{(1-\epsilon)^2\,\Sigma^2}{\epsilon^3}\,\mu\boldsymbol{u} + \beta \frac{(1-\epsilon)\,\Sigma^2}{\epsilon^3}\,\rho\boldsymbol{u}^2 \qquad (8)$$

with $\alpha$ = 150 and $\beta$ = 1.75. To describe the pressure drop across a bed of packed particles.

An alternative scale between the micro and macro model, corresponding to the meso-scale, was selected for this study to take advantage of information available at the pore scale without having to perform cumbersome and time-consuming simulations at this scale (see Section 3.3). For the meso-scale, a pore size limit is set to solve an averaged flow that will account for some of the micro-scale heterogeneity of the porous material using new 3D laboratory data from the med-CT and analysis techniques (Larmagnat et al., 2019). However, this consideration requires complex closure laws and a filtering procedure to bridge the two scales in order to estimate the permeability using meso-scale numerical simulations.

# 3. Methodology

## 3.1 Selection of materials

### 3.1.1 Glass bead models

For this study, an assembly of 269 spherical glass beads (16 ± 0.3 mm in diameter) was used to calibrate and validate different algorithms of image post-processing. A voxel (the 3D equivalent of a 2D pixel) edge of 0.4 mm (in z-axis, thus corresponding to the slice thickness) makes a sphere (glass bead) of radius equal to 40 voxels, equivalent to the size of a coarse sand grain/particle imaged via the micro-CT[1]. The sample size is thus 308 mm long and 68 mm in diameter.

### 3.1.2 Reference rock samples

The three reference core samples used is this study correspond to lithologies commonly used in studies by the hydrocarbon industry or in rock mechanics. The core samples are cylindrical and have a diameter of about 38 mm. Their exact dimensions and mean gas porosity estimated in a commercial laboratory are presented in Table 2.

The Berea sandstone is a medium-grained sandstone, Mississippian in age, which outcrops in Ohio (USA). It is mainly composed of quartz and feldspar with low clay content. Particles are well sorted and subangular with quartz overgrowths. The Boise sandstone is a medium to coarse-grained Late Miocene

[1] From a dimensionless point of view, studying a glass bead of 16 mm in diameter with the med-CT or a spherical sand grain of 100 microns with the micro-CT is the same, because only the number of points/voxels per diameter is important.

sandstone from Idaho (USA), which has a relatively high porosity (see Table 2). This sandstone is, nonetheless, poorly sorted and composed of quartz and feldspar, with minor clay content. The Indiana limestone is a middle Mississippian marine bioclastic carbonate that crops out in south-central Indiana (USA). The limestone is heterogeneous, with grainstone to packstone texture and is mostly composed of calcium carbonate with only a small amount of magnesium carbonate. Fossil fragments include bryozoans, echinoderms, and brachiopods.

Table 2: Size of the reference core samples used in this study, along with their estimated gas porosity.

| Rock type | Diameter (mm) | Length (mm) | Gas porosity* (%) |
|---|---|---|---|
| Berea sandstone (BE-K15B) | 38.0 | 51.0 | 19.3 |
| Boise sandstone (BO-K15B) | 37.8 | 49.1 | 33.6 |
| Indiana limestone (IN-C15A) | 37.7 | 99.0 | 16.3 |

Note: * The mean porosity of the samples was measured by an independent laboratory in Calgary (see Larmagnat et al., 2019).

## 3.2 Experimental measurements

### 3.2.1 Medical CT (med-CT) imaging

In this study, porosity datasets are derived from tomographic measurements made with a medical CT-scan (Siemens, SOMATOM, Definition AS128+). Specific scanning parameters were applied to each sample (Table 3).

Table 3: Scanning parameters used for both the glass-bead model and the two reference rock samples. kV stands for kilovoltage, mAs for milliampere-second and F.O.V stands for field of view (i.e., the size of the imaged volume).

| Parameter | Glass-bead model | Reference rock samples |
|---|---|---|
| kV | 100 | 140 |
| mAs | 200 | 350 |
| Collimation | - | 20x0.6 |
| Pitch | 0.9 | 0.55 |
| Rotation | 1s | 1s |
| Kernel | V80u | B70s |
| Scale | Normal | Extended |
| F.O.V. | 77 mm | 50 mm |
| Slice thickness | 0.4 mm | 0.6 mm |

For this study, the total and effective 3D porosity of each of these core samples was estimated using dry and saturated core samples, following the methodology of Larmagnat et al. (2019). This setup, including an in-house core-flooding setup, allows several individual core samples to be scanned in a dry or saturated state. Without any prior knowledge of samples (e.g., rock type, mineral composition), the three-dimensional alignment and subtraction of the two datasets (dry and saturated states) provide 3D connected porosity matrices. This methodology has been tested previously on a large set of reference cores and showed a strong correlation between mean core- porosity values obtained by CT-scan and those obtained by conventional gas porosimetry techniques (Larmagnat et al., 2019). The significant added value using med-CT- is the generation of 3D images of pore networks, allowing to assess spatial attributes of macropores and some contributions from the micro-pores, including their distribution and connectivity.

The datasets correspond to a series of cross-sectional images, which have to be processed and converted into a 3D computational mesh, so that the flow can eventually be simulated. Each series of X-ray images of a rock core sample has a dimension [nx,ny,nz] (where n is the number of voxels) and a resolution (i.e., spacing between pixels and cross-sectional images) [dx,dy,dz] (see Figure 4). Here, the idea is to post-process the raw X-ray images from the med-CT to identify the different phases (gas, liquid, rock) in the porous media.

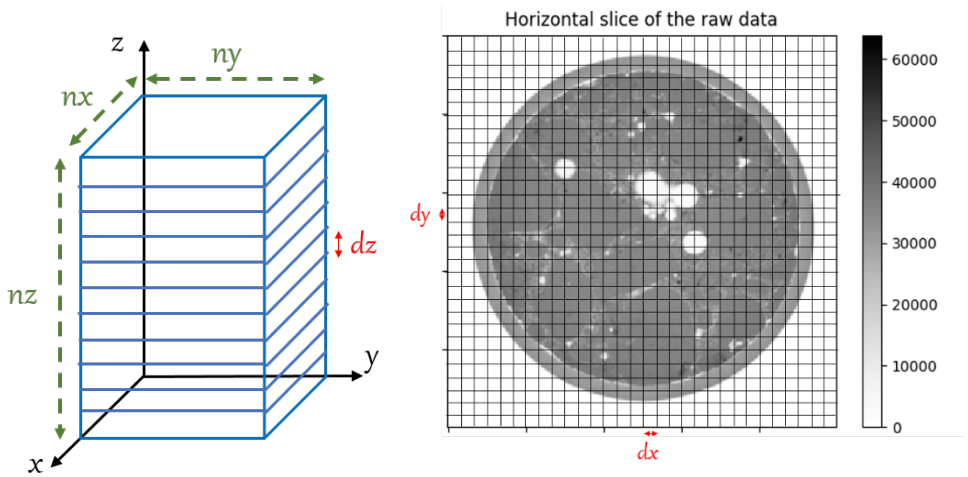


Figure 4: (a) Decomposition of the domain into layers of thickness dz. (b) Example of raw data from a horizontal slice of a micro X-ray CT scan of a concrete sample (Stamati et al., 2018a), where the color scale corresponds to a positive linear function of the Hounsfield Unit (HU), i.e. a quantitative scale for describing radiodensity.

Given the wide range of possible porosity values in natural porous materials and the impact of the type of porosity estimated to simulate the flow (Table 1; Figure 2), the selection of an appropriate material was crucial for this part of the study using med-CT, in order to obtain relevant results when generating the 3D geometry and mesh. Indeed, the pore and pore throat size must be large enough to be detected by the CT technique used, which constitutes a major limiting factor. Fine-grained rock core samples (such as shale, mudstone and siltstone) had therefore been ruled out from the outset for this part of the study.

### 3.2.2 Gas porosity and permeability measurements

Gas porosity and permeability measurements on core samples were made using the Core Test System AP-608 Gas permeameter-porosimeter at the Laboratoire Ouvert de Géothermie at INRS (Quebec City, QC). Prior to these analyses, samples were first dried at 108°C for at least 48 h, using a Thermolyne oven (Thermo Scientific). The AP-608 system is a conventional porosimeter applying Boyle's law, stating that for a fixed mass of an ideal gas (helium in this cas) at a fixed temperature, pressure is inversely proportional to the volume of the sample. Thus, measuring the change in helium pressure gives the grain volume. The porosity value is estimated from two measurements: grain volume and the bulk volume. A digital calliper was used to accurately measure the length and diameter to calculate the bulk sample volume. The permeability (k) was measured with the same instrument based on the transient pressure decay method. Results are expressed in $m^2$ or Darcy units. The permeability values were obtained with Darcy's law, and the Klinkenberg's correction for gas slippage was applied directly by the instrument. A confining pressure of 500 psig (3447.38 kPa) was applied for the permeability assessment.

## 3.3 Numerical modeling and prior validation

### 3.3.1 Prior validation using a glass bead assembly

A first step of this study was to verify the feasibility of generating 3D numerical domains using pre-existing medical CT-scan datasets of a near-ideal porous sample at the micro-scale (Hammouti et al., in preparation; Oukaili, 2019). This work included image processing and CFD mesh generation using a glass bead assembly. Its aim was to investigate the limits of the med-CT resolution and of the numerical methods, as well as the constraints related to computing power. Using the same set of med-CT images, both a micro-scale and a meso-scale approach were tested. Based on this work, the meso-scale approach appeared to be better adapted to the level of the experimental measurement datasets. This work is presented in Section 4, as an entire section needed to be devoted to this important step.

### 3.3.2 Selection of the scale

Based notably on the numerical experiment of Rakotonirina (2016), Rakotonirina et al. (under review) and previous work on the glass bead assembly, a new approach using a meso-scale was designed for this study to make the required image processing more automated and operational. The idea is to reduce the technical difficulties inherent to the generation of an intricate mesh, including the extracting and processing steps of CT-scan datasets (in this case 3D connected pore networks) and projecting them onto a simpler mesh to generate it. Given 1) the technical complexity of automatically transferring tomographic data (such as med-CT images) into a well-designed 3D mesh for pore-scale modeling applications and 2) the computational power required for mesh generation, a microscale approach had been rejected outright for our geological samples. Indeed, as presented in section 3.3.1, major technical difficulties were encountered using the pore (micro) scale even when using a quasi-ideal model (made of spherical glass beads). In the case of geological materials, the shapes are infinitely more complex and difficult to measure accurately, which complicates the generation of the mesh.

### 3.3.3 Mesoscopic modeling using glass beads and rock samples

Building upon the results obtained with glass beads, a further step was taken by applying the same approach to sedimentary rock images from three reference reservoir rock cores: a Berea sandstone sample, a Boise sandstone sample and an Indiana limestone sample (Table 2). The open-source software, Spam (Software for the practical analysis of materials, Stamati et al., 2020) was used for the post-processing of the CT-scan images, in particular for the analysis and manipulation of 2D and 3D datasets (Roubin et al., 2015; Stamati et al., 2020). The proposed workflow for this study is divided into two main steps, similar to the approach adopted for the glass-bead model.

First, raw X-ray images from the reference core materials (from Larmagnat et al., 2019) were used to obtain 3D connected pore networks, by comparing CT images in a saturated state and unsaturated state. Then, a segmentation procedure was applied to separate the solid matrix from the porous space. This approach by binarization was then investigated in order to evaluate at least some features of the microstructure of the porous media such as a statistical analysis of the pore distribution.

To investigate tortuosity, the Pytrax software was used. It is also an open-source Python library with an efficient random walk implementation highly parallelized for computing directional tortuosity (Tau) of tomographic images (Tranter et al., 2019). This calculation uses the reciprocal of the slope of the mean square displacement (MSD) and axial square displacement (ASD) as a function of time, which is

equal to unity in open space (i.e. without any path restrictions), once standardized [2]. From a thresholded image, the idea is to randomly introduce a designated number of "walkers" inside the pore space (here nw=1000 was used, where nw is the number of walkers) for a designated number of steps nt (here 1000) and to compute the displacement of all walkers for each orthogonal direction (ASD) and by averaging them using MSD.

The second step was to project the morphology onto the unstructured mesh. This procedure consisted first in calculating the distance fields (i.e., spatial fields of scalar distances to a given surface geometry) of each phase (material and voids), then in projecting these fields on a raw unstructured mesh. Further technical details can be found in Stamati et al. (2020).

# 4. Description of previous work on pore-scale modeling

## 4.1 Use of a glass-bead model

This section summarizes results of previous work (Hammouti et al., in preparation; Oukaili, 2019), where different approaches to simulate 3D fluid flow and heat transfer were tested using a quasi-ideal porous medium composed of glass beads, with porosity datasets obtained from a med-CT. The goal is to present a methodology adapted to the level of resolution of the med-CT measurements, the precision of the post-processing tools and the required computing power.

### 4.1.1. Image acquisition and segmentation

In the literature, there are many different tools available for processing images and extracting a structure (or phase) from med- and micro-CT datasets (Andrä et al., 2013a, b). The different open source and commercial software that were used in our previous work include Python and its Scikit-image (a collection of algorithms for image processing) and VTK-Visualization Toolkit, Fiji/ImageJ libraries and MATLAB. The MATLAB watershed function uses the Fernand Meyer algorithm (Meyer, 1994) and the Scikit-image library uses the ITK algorithm (Beare and Lehmann, 2006).

The first steps consisted in acquiring and processing med-CT images by "cleaning" scanned images (e.g. applying different filters to remove noise; Figure 5-Steps 1-2) then by binarizing the images to discriminate the solid matrix from the void space using a thresholding process (Figure 5-Step 3).

[2] Tau = t/N * 1/MSD$^2$, t being the number of time steps and N number of space steps.

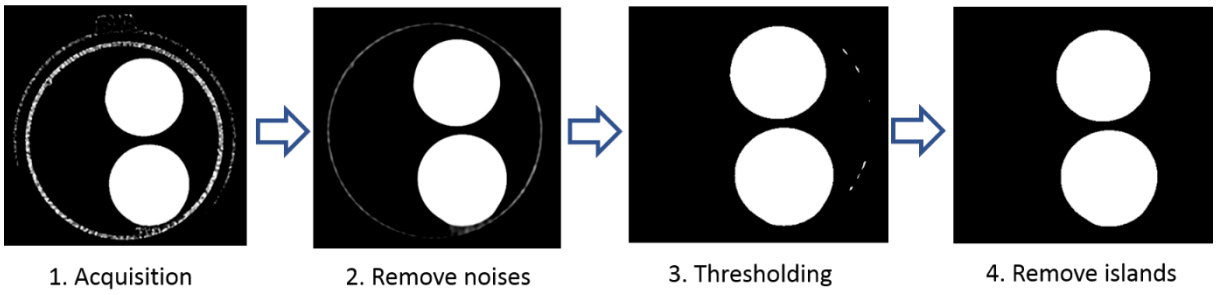


Figure 5: Illustration showing the workflow for image processing of glass-bead assembly (Oukaili, 2019).

The final step involved a post-processing phase to extract iso-surface in order to generate a STL-file (i.e., generic file used in stereolithography software for 3D representations) for each particle. This segmentation of the glass-bead configurations was made using a "watershed algorithm" (Beare and Lehmann, 2006), a widely used technique for image segmentation. This process is not straightforward depending on the shape of particles, and problems can occur even for the "simple" case of spherical shapes. For instance, the configuration of particle-particle contact can be ignored by the algorithm, which considers two particles as a single particle with a "peanut shape". Therefore, several solutions allow to upgrade the efficiency of the object segmentation at each step of the process. An example is provided in Figure 6 showing how two particles in contact (overlapping) are processed with a distance transform method. In this case, a distance transform Watershed algorithm was used for segmentation (see section 4.2).

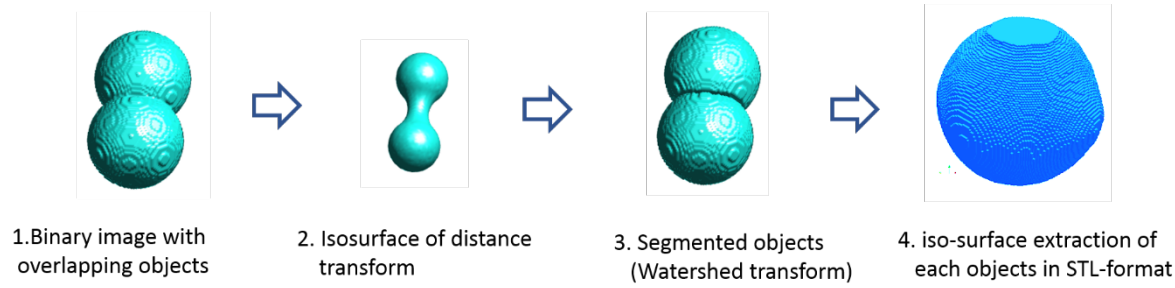


Figure 6: Illustration of the different stages of object segmentation using the Watershed algorithm in MATLAB (from Oukaili, 2019).

### 4.1.2. Meshing the pore space

In order for the Navier–Stokes equations to be correctly solved for the fluid domain, the pore space must be well resolved, including the definition of the fluid-solid interfaces and the computation of surface normals. Computing the detailed kinematics of flow through discrete pores is a complex task for the following three main reasons:

1. The generation of a porous medium geometry from a raw X-ray image is not straightforward. As explained in Section 4.1, various image processing (binarization, segmentation, etc.) are necessary to make the geometry usable;
2. The geometry of the pore space domain where the fluid circulates is complex (corresponding to a tortuous network of non-symmetric pores), which leads to issues in generating the mesh of this domain;
3. The scale at which porosity and tortuosity are studied can lead to non-Darcian flow.

In Oukaili (2019) and Hammouti et al. (in preparation), these issues were investigated from a micro-scale perspective. Even though the sample studied is actually centimetric in size (with the beads having an average diameter of 16 mm), the 269 glass-bead assembly is a micro-scale analogue of a porous medium because each particle (bead) and/or pore space/throat can be identified at the med-CT resolution.

Even though the glass bead assembly is a near-ideal medium and an automated process is used to generate the mesh, the outputs are not always consistent. As explained in section 4.1, this is related to the choice of binary image processing and the segmentation process accuracy (here, the Watershed algorithm) to preserve the original particle shape and, consequently, to the operator inputs (such as filters imposed for particle smoothing, spatial resolution step, etc.) on which a proper transfer of the iso-surface geometry into a pore space mesh depends.

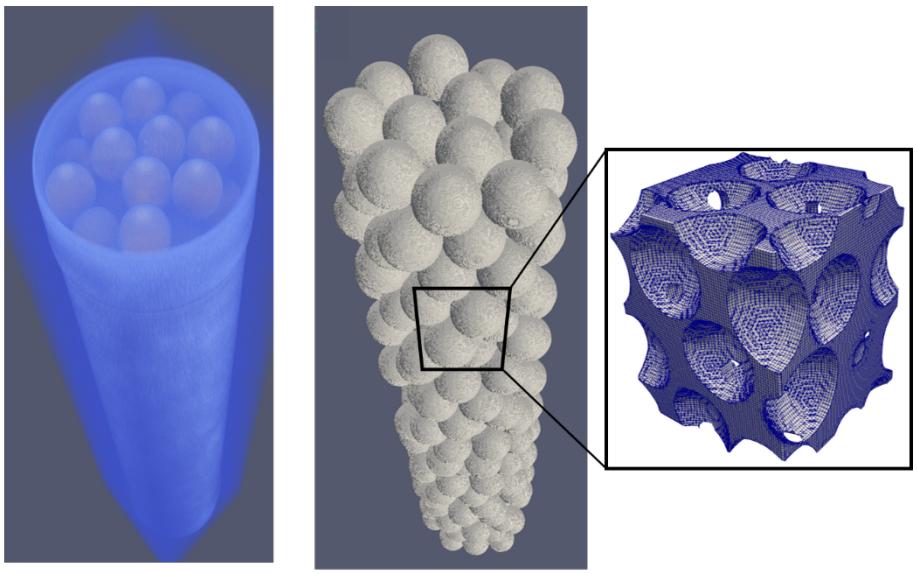


Figure 7: Illustrations of the 269 glass-bead assembly showing three different stages of the workflow (Hammouti et al., in preparation): (a) A TIFF-file after med-CT scanning (b) An STL-file after the 1-2% reduction of each glass bead (c) DEM (data exchange mode) file showing an area inside the fluid domain generated after meshing.

As an indication, the dataset generated from the med-CT images of the glass-bead assembly illustrated in Figure 7a contains 200 million voxels. If the med-CT datasets were processed as is (i.e., with each voxel considered either as glass material or pore space), post-processing would take several hours or even days. To avoid this long iterative procedure, an alternative solution was used, where each glass-bead is considered separately using the Watershed algorithm in combination with an erosion (or shrinking) algorithm (Figure 7b). The latter is used to reduce the diameter of each glass bead by about 1% to 2% to ensure a clear separation of the convex contact region and, therefore, the identification of the discrete pore space (see Figure 8).

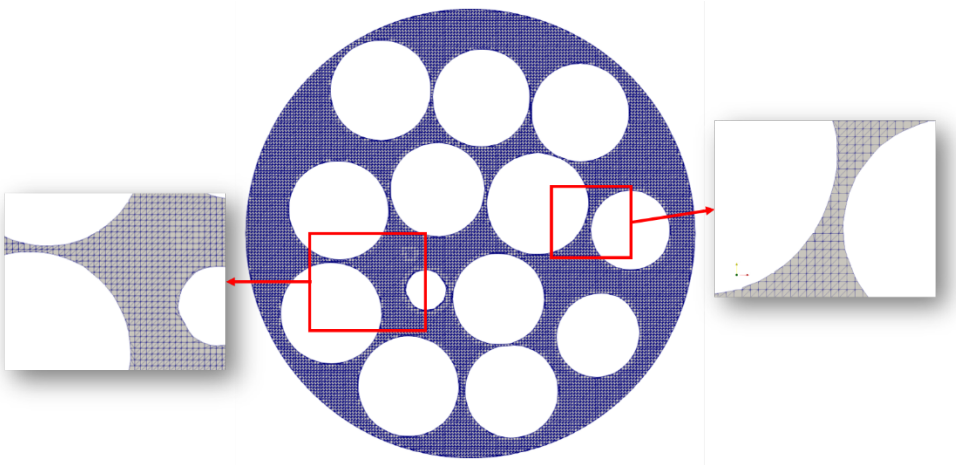

Figure 8: Cross-section of the mesh of a sample composed of glass beads scanned with the med CT-scan (Hammouti et al., in preparation). The mesh was generated using the Salome software. This illustrates how the erosion algorithm helps the mesh generator by slightly increasing the space between the particles (here beads), ensuring that at least one voxel separates each particle. Note: The beads have all the same diameter (16 mm ± 3%), but since this cross-section shows a xy plane, the beads are not all cut in their center.

### 4.1.3. Coupling of hydrodynamic flow with heat transfer

To implement the numerical coupling between the porous medium, the hydrodynamic flow and the heat transfer, the Code_Saturne, an open-source software developed and distributed by EDF (Électricité de France) to solve computational fluid dynamics (CFD) applications, was used. This code uses a finite volume method that allows the use of an unstructured mesh, thus optimizing the mesh construction process for complex geometries. This numerical tool solves the 3D time-dependent Navier–Stokes equations to obtain results for the simultaneous resolution of the fluid velocity and pressure as a function of position and time. In order to estimate the deviations and errors resulting from the mesh generation, two configurations were compared: one composed of numerically

generated particles using a Discrete Element Method (Figure 9a) and the other composed of the scanned glass bead assembly (Figure 9b).

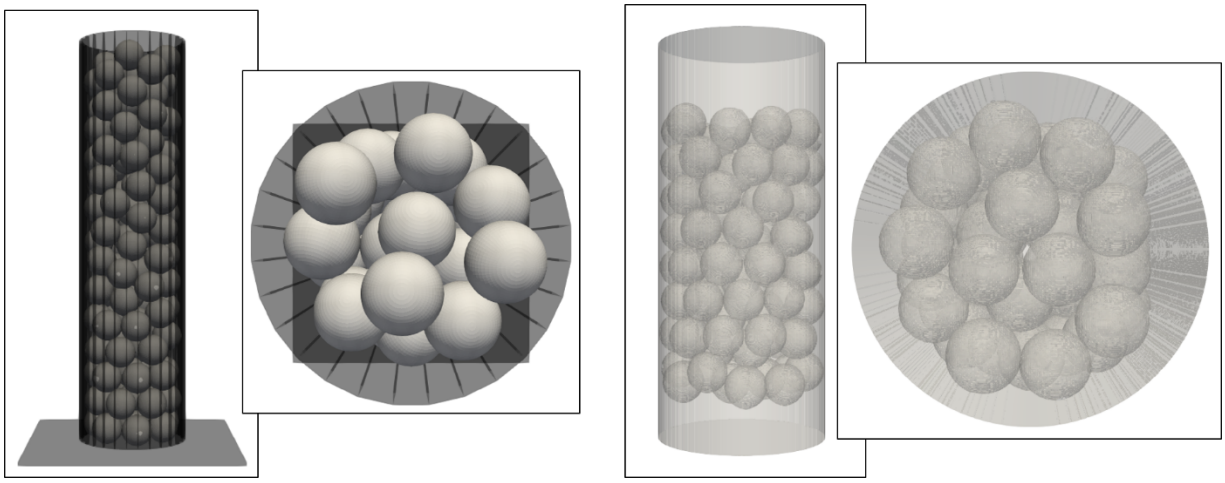

(a) (b)

Figure 9: (a) Configuration of an assembly of spherical particles generated numerically using a DEM (Discrete Element Method) (b) Configuration of a scanned assembly made of 269 glass beads (medical CT-scan images). Taken from Hammouti et al. (in preparation).

Figure 10 shows an example of the results of the flow and heat transfer simulations through a cylindrical porous medium composed of 269 spherical particles generated from the DEM model. To minimize the memory size for the mesh and the computational time, (only the first 110 particles from the pile of 269 glass beads shown in Figure 7 (and Figure 9b) were selected for the simulations. The boundary conditions were as follows:

(i) No-slip wall boundary condition (i.e., **u** = 0 was applied to the lateral cylinder wall);

(ii) a uniform upward inlet velocity and a constant (Dirichlet) temperature were applied to the bottom of the cylinder;

(iii) a zero outlet pressure and a zero outflow boundary condition for the velocity and temperature were applied at the top of the cylinder.

This set up, imposing a flow regime, allowed the computation of an upward (bottom-up) flow in the cylinder. The simulations for this cylinder containing 110 spherical particles required 4 million cells, and took 72 hours of computation using 8 cores (individual processing units).

Figure 10 shows 2D and 1D cross-sections for the dimensionless velocity and temperature fields for a x=2.5 cm cut plane (left image for a and b, respectively) and 1D-profiles for velocity, pressure (right-a) and temperature (right-b) along the z-axis for x= 2.5 cm and y=3.5 cm. There are no glass beads at the

top and bottom, as suggested Dorai (2015), to avoid edge effects in the calculation of porosity (see Section 5.2.1). While the 1D pressure-profile shows a general pressure drop that is quite linear, the 1D and 2D velocity profiles show large overshoots (up to 7 times the imposed velocity) especially between particles and at the particles/cylinder wall interface that is due to the Venturi effect (according to the principle of mass continuity, an incompressible fluid velocity must increase as it passes through a constriction). For the temperature fields, the 1D and 2D profiles clearly show the progression of the temperature front, which has not yet diffused into every pore, and the temperature drop in the wake of the particles at the top of the cylinder.

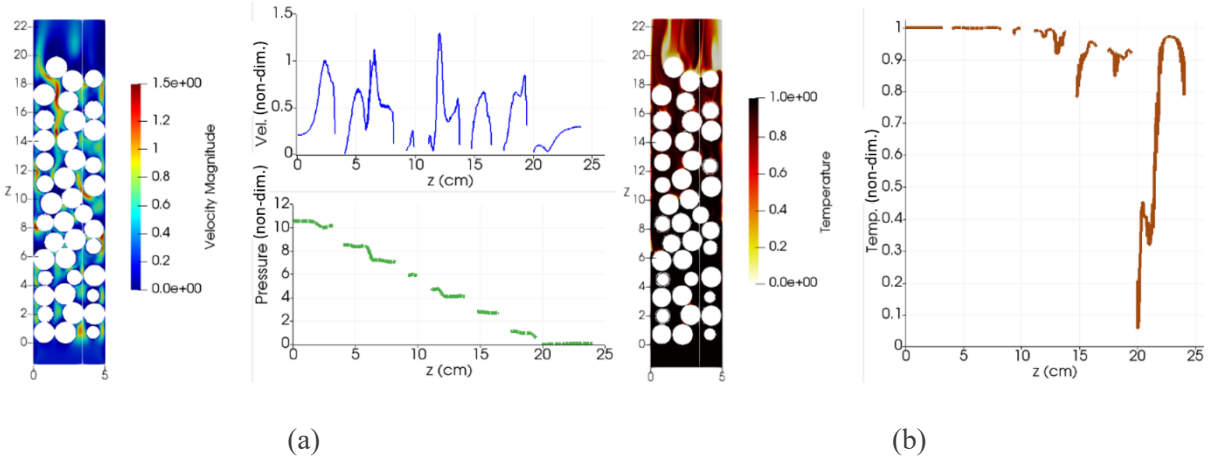


Figure 10: Results of numerical simulations for flow through a cylinder containing 110 spherical particles, where velocity (**u**) and temperature (T) fields are imposed through boundary conditions at the bottom (u=0.2 and T=1) and at the top (du/dz=0, dT/dz=0 and p=0). All fields (velocity and pressure) are dimensionless. (a) Velocity and pressure profiles are provided along the z-axis for x= 2.5 cm and y=3.5 cm). (b) Temperature profile along the z-axis also for x= 2.5 cm and y=3.5 cm. Figures are adapted from Hammouti et al. (in preparation) and Oukaili (2019).

## 4.2. Use of a concrete sample

Configurations of isolated pores have previously been studied using concrete core samples and Spam, a platform using the Python/C++ language (Roubin et al. 2015, Stamati et al., 2018a; 2018b). These results are available directly on the platform Spam, including images obtained with a micro-CT scan (with no saturation protocol). The porosity of concrete samples has been investigated with a multiphase material approach, demonstrating the feasibilty of studying heterogeneous materials containing both micro and macro-pores. Somewhat similar to a rock core sample, the concrete cement core sample indeed represents a complex case, where three phases are present, as this material consists of a mixture of aggregates (sand and gravel) contained in a paste (mortar), composed of cement and water. Typically, concrete is a mixture of about 10-15% cement, 60-75% aggregates and 15-20% water; entrained air is often present and may also occupy an additional 5-8%. The pore space is poorly connected, since concrete is supposed to be (almost) impermeable, which plays an important

role in its durability. Figure 11 presents an example of an X-ray image where the three phases inside the concrete sample are identified, based on a dataset made available by Spam developers. Phase labelled #2 (medium-dark grey) corresponds to pores well resolved by micro-CT imaging.

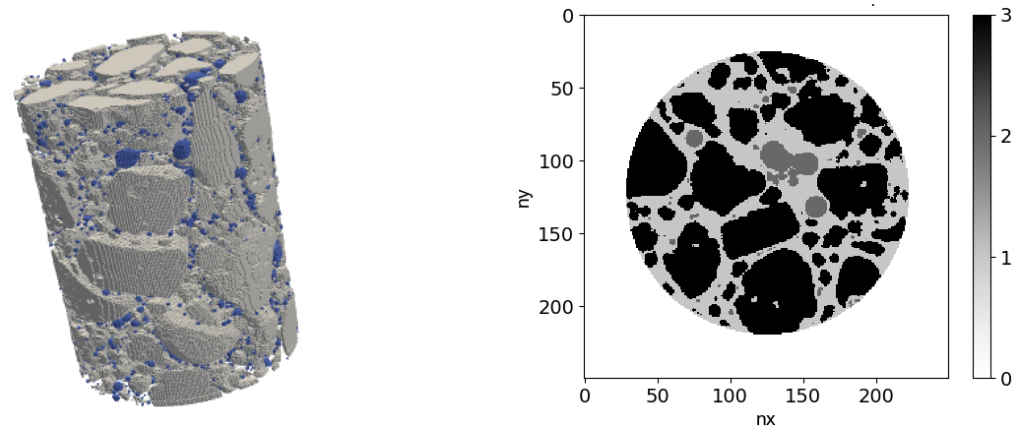


(a) (b)

Figure 11: Images of a scanned concrete sample, generated from a micro-CT dataset made available by Stamati et al. (2018a). (a) 3D trinary image - blue: macro- and micro-pores, light grey: aggregates and the rest is occupied by the mortar matrix. (b) Horizontal slice at the middle of the sample showing the identified phases. Phase 0 (white): outside the media, phase 1: mortar, phase 2: pores, phase 3 (black): aggregates. X-ray image dimensions are [nx,ny,nz]=[250,250,400] and resolution dx=dy=dz=0.055 mm.

Concrete is a very heterogeneous material (as highlithted by Figure 11 and Figure 12), both in terms of pore and grain size, geometry and spatial distribution. Total porosity varies along the sample from nearly 0 to 8.5%, with an average of 2.76% (Figure 12b). Concrete samples do not (and should not!) contain connected porosity and, therefore, will not be used as an example to study fluid flow through porous medium.

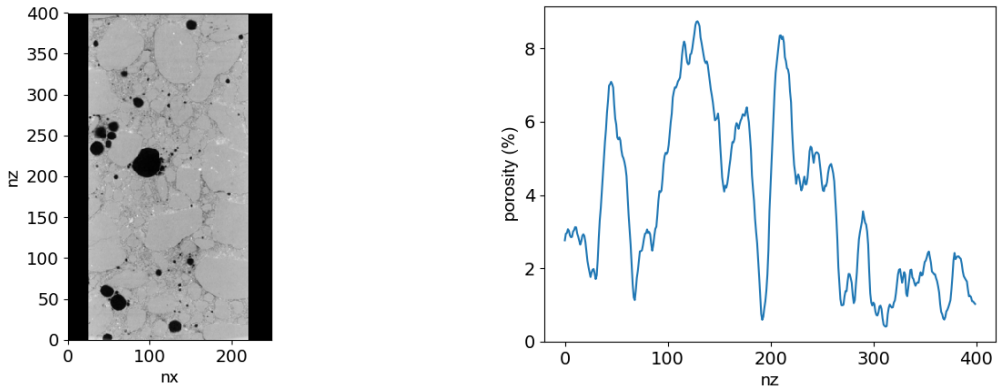


(a) (b)

Figure 12: (a) Longitudinal view (x-z plane) of the concrete sample from Stamati (2018a). b) Total porosity profile averaged for each x-y plane plotted along the z-axis. The average total porosity is 2.76%.

# 5. Estimation of effective porosity and preparation for flow modeling work at the meso-scale

## 5.1. Phase identification and porosity estimation

The post-processing tools of Spam, which allow both the identification of the different phases (voids/pores and solids/grains) of a sample and their projection onto an unstructured mesh (previously built), was also used in this study. This post-processing approach can be used for our set of reservoir rock samples, allowing us to separate the contributions of connected pores (since only the effective porosity is of interest in this study) from the solid matrix and hence prepare 3D models for subsequent flow simulations. However, since this platform was initiatially developed to study structural mechanics issues (e.g. the deformations and stresses of civil engineering structures), some adaptations and/or modifications were necessary for the coupling with our simulations of fluid flow and heat transfer. Of note, it was not possible to identify isolated pores of the three geomaterials available for this study from the med-CT images post-processed with Spam, due to the saturation technique used.

## 5.2. Effective porosity

Based on the experience gained using the dataset from the concrete sample case study, the same approach was first applied to the glass bead assembly, then to the three reference core samples (which are described in section 3.1.2). In Larmagnat et al. (2019), a data analysis on these reference core samples performed by comparing saturated and dry state from medical CT images allowed the definition of the connected macropore network, providing an evaluation of the 3D effective porosity distribution. Using the same med-CT dataset, the three selected core samples were binarized so that there were only two distinct phases to consider: the interconnected porous phase (i.e., where the air space in the dry state has been replaced by water in the saturated state, thus corresponding to the connected porosity) and the solid (or matrix) phase.

### 5.2.1. Case study of a near-ideal porous medium: the glass bead assembly

The use of a near-ideal porous medium provided a case study allowing us to control the porosity and the connectivity of the pores. Such near-ideal models, typically made of glass beads (mono or polydisperse spheres), have been the subject of numerous scientific studies (Dorai, 2015; Hammouti et al., in preparation; Kutsovsky et al., 1996; Patel et al., 2019). From these studies, both analytical and empirical data are available to validate our models, which represents a significant advantage. Using the glass bead model described in section 3.1.1 and previously studied (see Section 4.1), the Spam workflow was applied and Figure 13 presents the identified phases (interconnected pores and solid matrix).

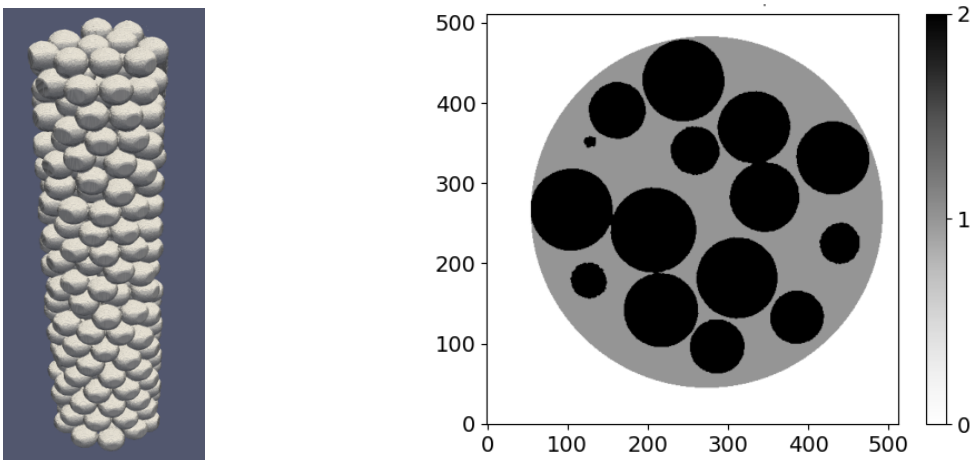


(a) (b)

Figure 13: Glass-bead assembly - (a) STL-file of the 269 glass-bead assembly, with dimensions [nx,ny,nz]=[512,512,771] and resolutions of dx=dy=0.15mm and dz=0.4mm (obtained with the medical CT-Scan). (b) Horizontal slice showing the identified phases (mid sample) – phase 0: outside the media, phase 1: interconnected pore space, phase 2: glass beads (Hammouti et al., in preparation).

To avoid edge effects in the calculation of porosity, Dorai (2015) suggests removing the equivalent of three sphere diameters at the top and bottom of the assembly. Under this condition and after binarization, the glass bead assembly sample (neglecting the top and bottom parts) has an average total porosity of 46.52% and an average effective porosity of 44.07%. The porosity profile in Figure 14b shows effective porosity ranging generally between 32% and 50% across the sample.

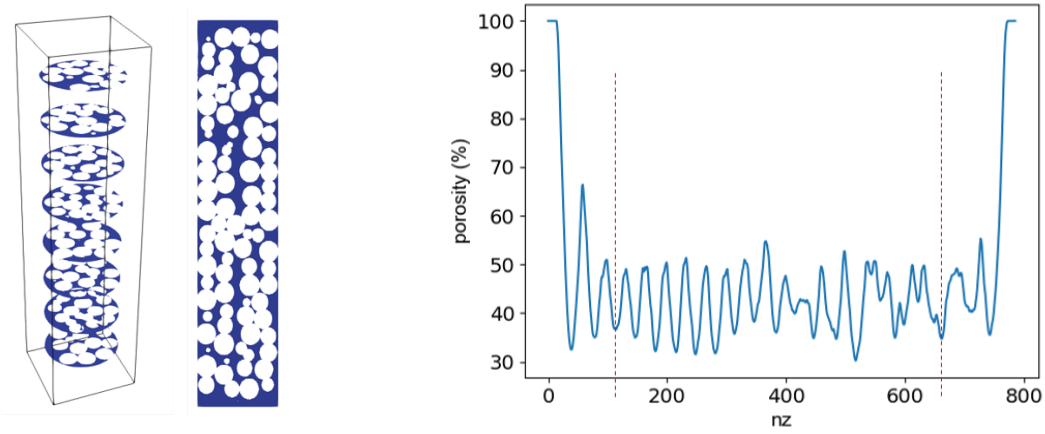


(a) (b)

Figure 14: Glass-bead assembly - (a) Lateral (x-z) and radial (x-y) planes of the glass bead sample showing the pore space, taken from Hammouti et al. (in preparation) (b) Porosity profile of this sample, after binarization and removal of a top and bottom layer equivalent to 3 times the average sphere diameter (red dotted lines).

Following the methodology of Oukaili (2019), this med-CT dataset was binarized using the Spam software (Figure 15a-b), then an image segmentation algorithm was applied (Otsu, 1979). The Otsu algorithm from the Scikit-image (image processing library in Python) was later used to perform automatic image thresholding, separating voxels into two classes, glass bead matrix and void space.

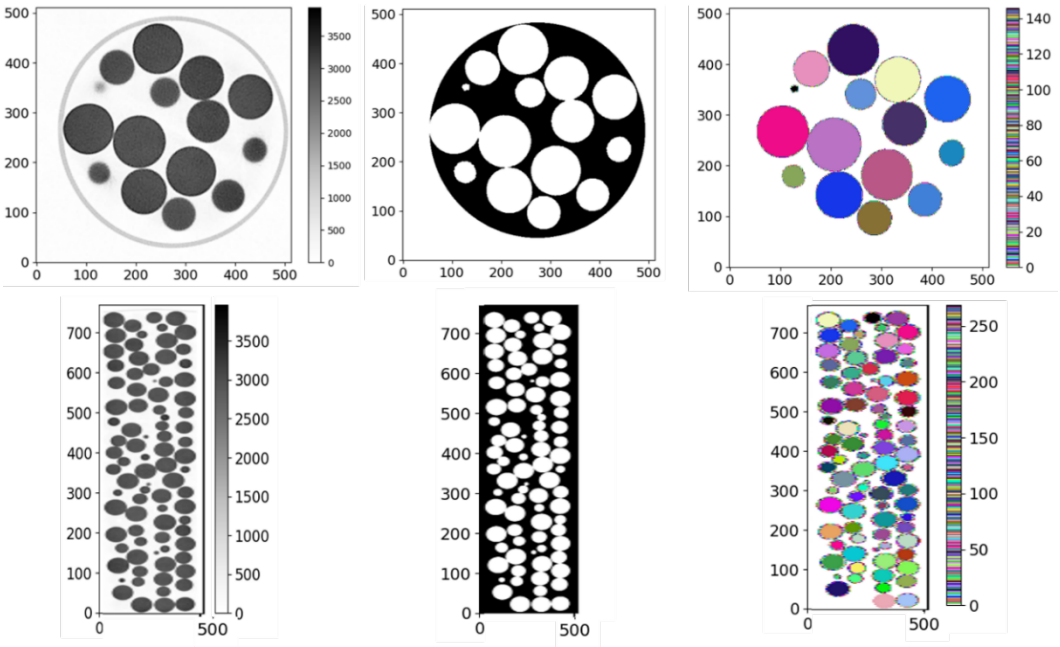

(a) Raw data (b) After binarization (c) After Watershed segmentation

Figure 15: Glass-bead assembly - Representation of the pore network of the 269 glass-bead assembly along slice 385 for the x-y axis and slice 256 for the x-z axis. a) raw data, b) after binarization using Otsu's algorithm (Otsu, 1979) and (c) after segmentation using the ITK Watershed algorithm to separate the glass beads.

The implementation of the ITK Watershed algorithm (Figure 15c) allows the separation of each glass bead and the evaluation of the distribution of their size within the sample, as the glass beads are not all exactly 16 mm in diameter due to the tolerance size. The estimated distribution provided an average volume of 2070 $mm^3$ for each bead, while a perfect 16 mm bead corresponds to a volume of 2144.6 $mm^3$ (Figure 16).

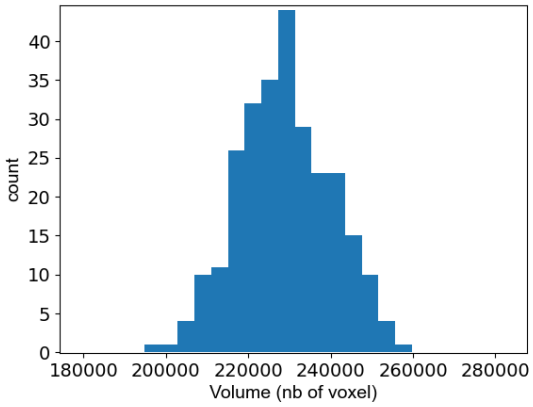


Figure 16: Glass-bead assembly - Statistical distribution of the glass bead size within the sample obtained using the ITK Watershed algorithm. A total of 269 glass beads were identified. The minimum glass bead volume is 196 611 voxels (corresponding to 1769.5 $mm^3$) and the maximum glass bead volume is 260 936 voxels (2348.4 $mm^3$). 1 voxel = dx*dy*dz. Of note, a maximum tolerance of $\varepsilon_{tol} = 3\%$ on the diameter leads to a maximum of $\varepsilon_{tol}^3 = 27\%$ on the volume.

Tortuosity using the Pytrax software was then investigated. Figure 17 shows the results obtained for the glass bead assembly in all three dimensions (x, y, z). A perfectly isotropic sample would show an overlap of all curves with a slope equal to 1 (i.e., a tortuosity Tau=1). Here, some differences are observed in the axial square displacement (ASD), especially between the longitudinal axis (z-axis) and the radial axes (x and y axis). The fact that the sample is much more “confined”[3] (with respect to wall effects) in the xy direction than in the z direction plays a role. Figure 17 demonstrates that even for a quasi-ideal model made of (nearly) identical glass beads, tortuosity is quite significant.

[3] A bead assembly is said to be "confined" when the ratio D/d is smaller than 10, where d is the diameter of the beads and D is the diameter of the cylinder that contains them.

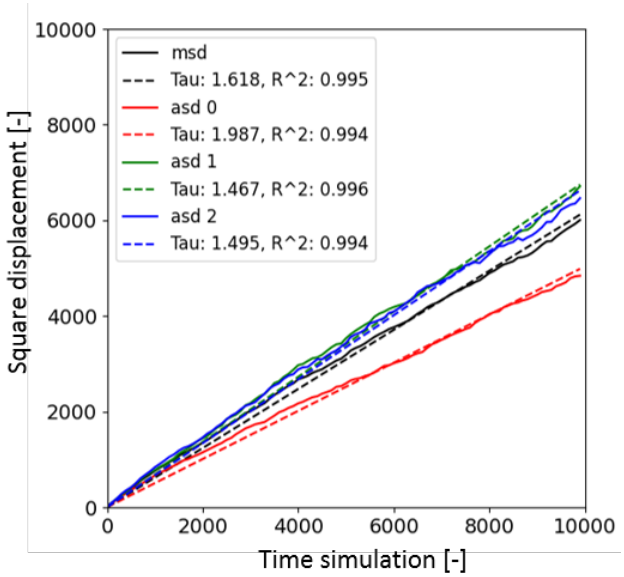


Figure 17: Glass-bead assembly - Mean (MSD) and axial (ASD) square displacement for the different axes (0: z-axis 1: x-axis 2: y-axis) versus time. The plain lines represent the actual results and the dotted lines are the linear regressions for which the slope defines the tortuosity (Tau). The higher the square displacement over time, the lower the tortuosity (since the fluid takes a shorter path to pass through the sample).

### 5.2.2. Boise sandstone core sample

The Boise sandstone (BO-K15B) is a medium to coarse-grained, poorly sorted sandstone mainly composed of quartz and feldspar minerals, with minor clay content. Based on the work of Larmagnat et al. (2019), the connected pore network was obtained by subtracting med-CT images from saturated and dry states (see section 3.2.1, these datasets are hereafter called “subtracted datasets”). However, one or two voxels were removed from the Boise sandstone imagery along the sample length and its diameter to avoid edge effects due to the sample cutting (Figure 18a). The subtracted dataset was binarized using Spam software and workflow. A 3D view and a transversal slice are presented for comparison in Figure 18b and c.

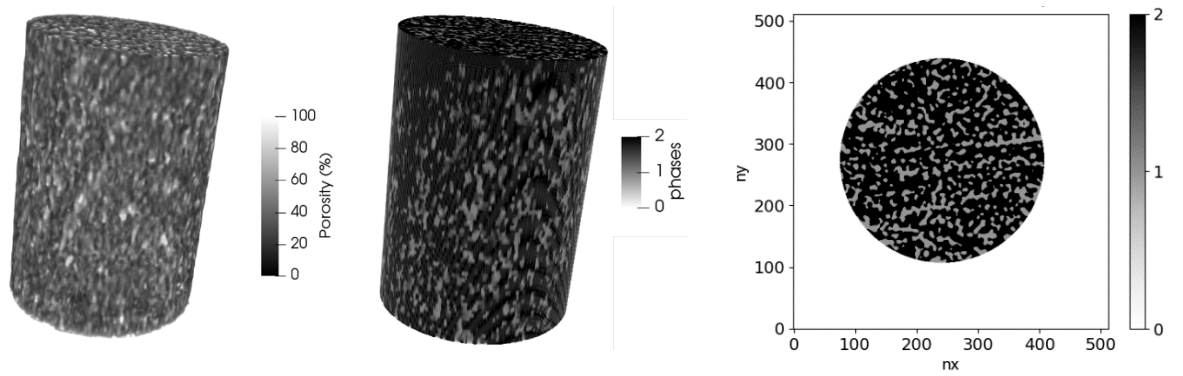


(a) (b) (c)

Figure 18: Boise sample (BO-K15B) with dimensions [nx,ny,nz]=[512,512,78] and resolution dx=dy=0.1mm and dz=0.6 mm (a) 3D view of the connected porosity network estimated using med-CT images from saturated and dry states, from Larmagnat, et al. (2019). The grey scale indicates the amount of water replacing air in the sample: from 0% (black, i.e., a voxel completely occupied by the geomaterial) to 100% (white, i.e., a voxel completely occupied by a pore). (b) 3D view illustrating binarized med-CT images using Spam and (c) transversal slice through the binarized dataset showing the different phases (in the middle of the sample) – phase 0 (white): outside the media, phase 1 (grey): pores, phase 2 (black): matrix. Note: When presenting binarized results, Spam uses a continuous scale, although only three values (0, 1 and 2) are actually used.

In terms of macropore size and distribution, the connected pore network of the Boise sample (BO-K15B, Figure 18a) appears to have a relatively homogenous macropore distribution in the axial section, based on the visualization of 78 cross-sections from the subtracted dataset. Figure 18c provides an example of these sections at the middle of the sample. To confirm the heterogenous distribution of macropores along the z axis, the mean porosity of each z-cross section was measured to obtain the effective porosity profile across the sample (Figure 19). The effective porosity directly obtained from the "subtracted dataset" ranges between 30.0% and 31.3%, with a mean porosity of 30.8%, while the binarized effective porosity ranges between 28.0% and 31.5%, with a mean porosity of 30.2%[4]. The average values obtained from the binarized and non binarized datasets are thus about 3% lower than the one obtained with gas porosimetry (33.6%) (published in Larmagnat et al., 2019). When comparing porosity profiles (Figure 19), the Boise sample shows a good correlation between the effective porosity obtained from the binarized and the non binarized datasets.

[4] For binarized datasets, a voxel is worth 0 (solid) or 1 (pore), while for subtracted (non-binarized) datasets, a voxel is worth from 0 to 1. To calculate porosity, all voxels are summed to obtain the total pore volume.

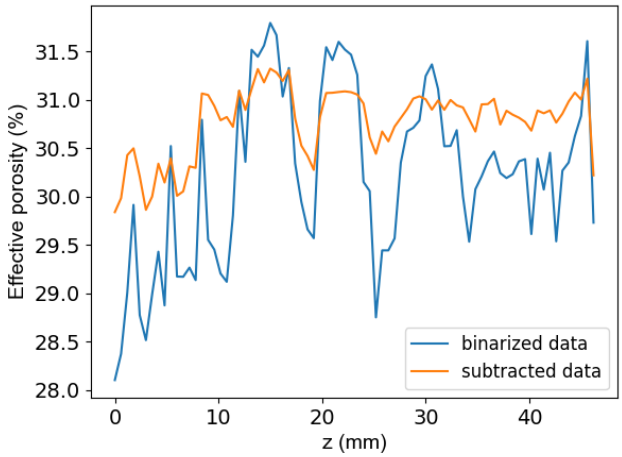


Figure 19: Boise sandstone sample - Porosity profiles along the sample (z in mm). Although the values are more variable in the case of the binarized dataset, average values are very similar for the subtracted (30.8%) and binarized datasets (30.2%).

To compare porosity after each step of the process, Figure 20 provides both cross-sections (x-y axis) and longitudinal sections (x-z axis) of the subtracted dataset, after its binarisation and then segmentation. The subtracted and binarised datasets show slightly variable values across the sample (respectively a standard deviation $\sigma \approx 0.9\%$ and $\sigma \approx 0.4\%$, as estimated from Figure 19). A careful comparison between the subtracted and the binarized datasets, for various longitudinal slices, shows that the binarization process slightly expand macropores and connections between macropores in some places or, conversely, neglects microporous areas that end up being labelled as rock matrix. This result is not surprising because the binarization process modify the microstructure of porous media by acting like a “steep” filter[5].

[5] In reference to the filter in signal processing or in electronics: filters act by dividing the frequency range into steps (0 and 1 in a steep way). Binarization proceeds in the same way (white or black, i.e., porous or solid).

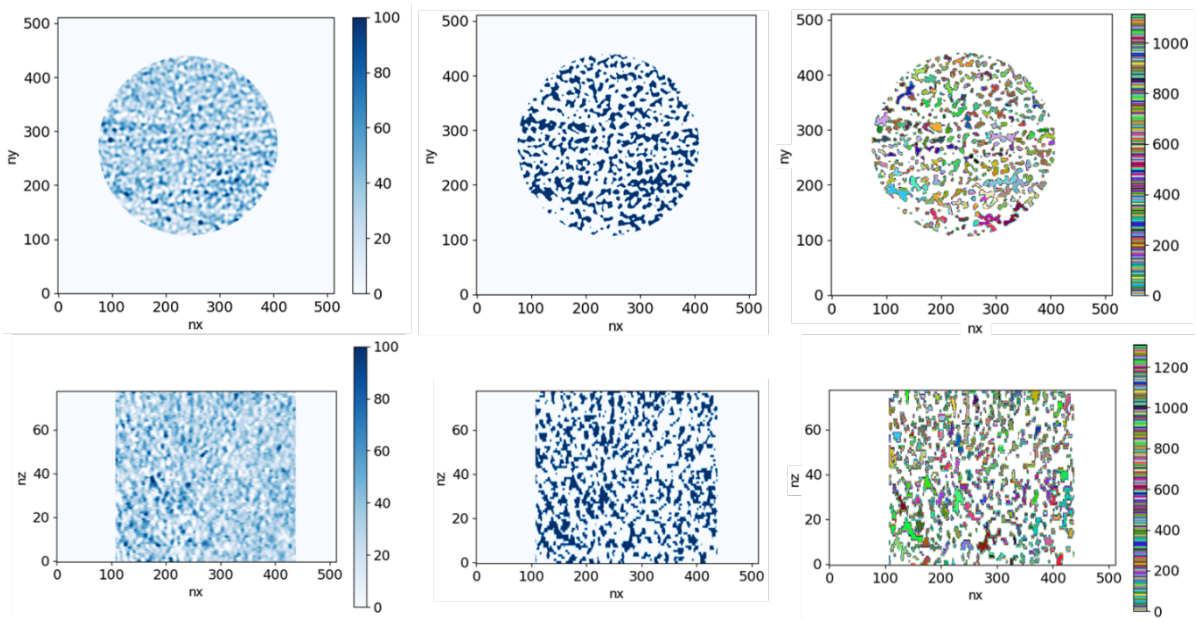


(a) Subtracted dataset (b) After binarization (c) After Watershed segmentation

Figure 20: Boise sandstone sample - Representation of the pore network along slice 41 for the x-y axis and slice 256 for the x-z axis. a) Subtracted data: The blue scale indicates the amount of water (from 0% (white, i.e. a voxel with no pore) to 100% (white, i.e. a voxel completely occupied by a pore), b) after binarization (dark blue: pores, white: matrix) using Otsu's method (Otsu, 1979) and (c) after segmentation using the ITK Watershed algorithm to separate macropores.

Segmentation on the binarized dataset using the ITK Watershed algorithm (Figure 20c), to allow the separation of the pores to count them as separate objects, suggests that the pore size distribution within the Boise sandstone is heterogeneous, which is confirmed in Figures 21 and 22. The largest pore population is moderate in size (around 1000 voxels), but there are also a good number of large to very large pores (Figure 21). A total of 1327 (macro) pores were identified. The mean pore volume is 1536 voxels (i.e., 9.21 $mm^3$), and the median equals 1092 voxels (6.55 $mm^3$), with a minimum pore volume of 15 voxels (0.09 $mm^3$) and a maximum pore volume of 12 212 voxels (73.27 $mm^3$).

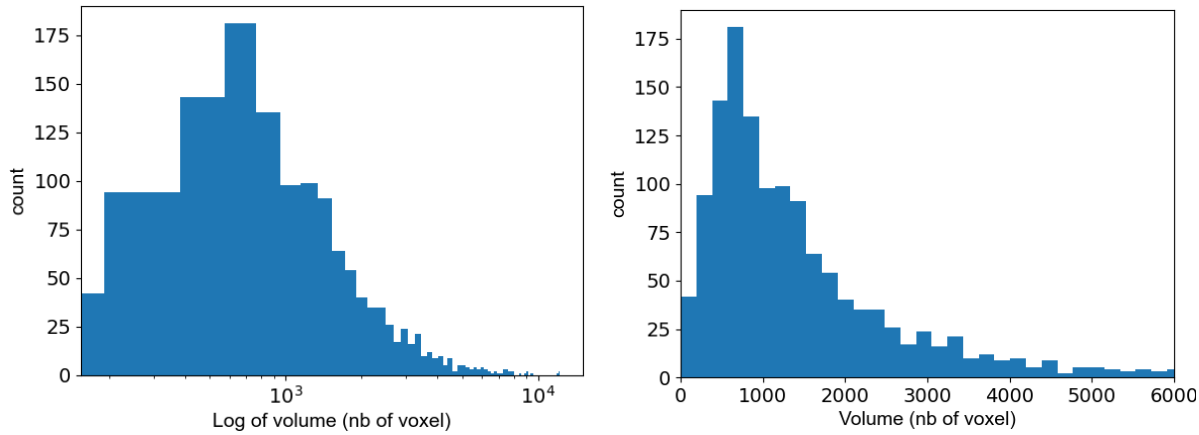


(a) (b)

Figure 21: Boise sandstone sample - Statistical distribution of the (macro) pore size of the Boise sandstone using the ITK Watershed algorithm: a) semi-log plot presenting the entire population b) linear plot best showing the majority of the population.

Unlike the case of glass beads where all the pores are interconnected, geomaterials can have dead ends. To quantify this feature, which has major implications for fluid flow, tortuosity estimation provides a good indicator. The tortuosity analysis (see Figure 22) shows that the mean tortuosity factor of the Boise sandstone is around 5.1 with a clear anisotropy in all directions, especially between the z-axis tortuosity (Tau=11.9) and the xy-axis tortuosity ($3.2 \leq Tau \leq 5$). This significant difference can probably be attributed, at least to a large part, to the depositional and consolidation processes that may have generated many more dead-ends in the vertical direction than in the horizonal (x-y) direction. Fluid flow simulations will allow us to confirm or refute this hypothesis.

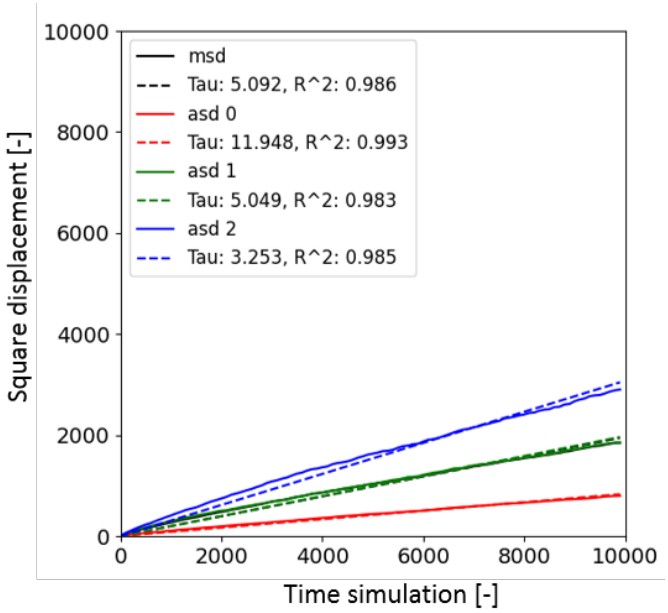


Figure 22: Boise sandstone sample - Mean (MSD) and axial (ASD) square displacement (0: z-axis 1: x-axis 2: y-axis) versus time for the Boise sandstone sample. The plain lines represent the actual results and the dotted lines are the linear regressions for which the slope defines the tortuosity (Tau).

### 5.2.3. Berea sandstone core sample

For the Berea sandstone, Larmagnat et al. (2019) found an average effective porosity value of 19.3% (Table 2). Figure 23 (b and c) presents a 3D view of the sample and a cross-section resulting from the binarizarion of this med-CT dataset.

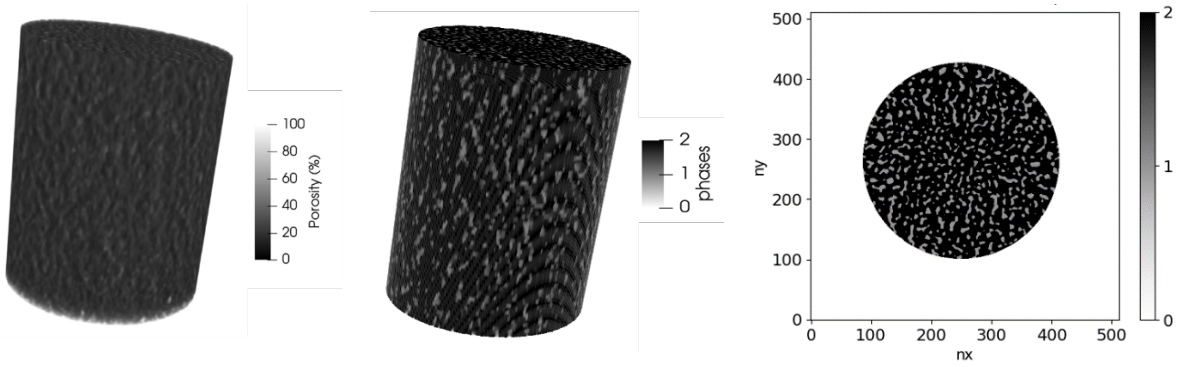


(a) (b) (c)

Figure 23: Berea sample (BE-K15B) with dimensions [nx,ny,nz]=[512,512,78] and resolution dx=dy=0.1mm and dz=0.6mm. (a) 3D view of the connected porosity network estimated using med-CT images from saturated and dry states, from Larmagnat, et al. (2019). The grey scale indicates the amount of water replacing air in the sample: from 0% (black, i.e., a voxel completely occupied by the geomaterial) to 100% (white, i.e. a voxel completely occupied by a pore). (b) 3D view illustrating binarized med-CT images using Spam and (c) transversal slice through the binarized dataset showing the different phases (in the middle of the sample) – phase 0 (white): outside the media, phase 1 (grey): pores, phase 2 (black): matrix. Note: When presenting binarized results, Spam uses a continuous scale, although only three values (0, 1 and 2) are actually used.

In terms of macropore size and distribution (based on the visualization of 78 cross-sections generated from the subtracted dataset), this Berea sample (BE-K15B), shows an uneven distribution of macropores, with an apparent less porous area in the middle of the core sample (see Figure 23c). The effective porosity profile from the binarized dataset (Figure 24, blue line) shows values ranging between 15.5% and 19.0% with a mean porosity value of 17.3%, while values for the subtracted dataset range between 18.8% and 19.8%, with a mean of 19.3%. Again, values obtained with the binarized dataset are more variable, suggesting that binarization may overestimate or underestimate (in other cases) effective porosity by sometimes mislabelling microporous areas (not fully resolved by the med-CT) as macropores or grains. Overestimation of individual pore sizes can occur, for example, if several pores are joined together during the binarization process, while underestimation occurs when small pores are erroneously associated with matrix grains (because not seen by med-CT). Also, the binarized dataset shows a fairly significant increase along the z-axis. This increasing trend could come from a slight angle introduced during the alignment when subtracting the wet and dry samples (for the dataset construction). This slight angle of deviation would not be visible on the subtracted dataset, but would likely be amplified (multiplied) during the binarization process. Nevertheless, the average value of the binarized dataset is 17.3%, which is only slightly lower than those obtained from the subtracted dataset (19.3%) and gas porosimetry (18.9%, from Larmagnat et al. (2019).

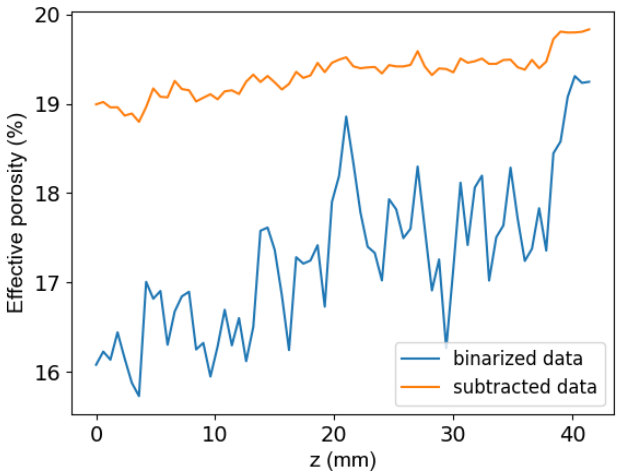


Figure 24: Berea sandstone sample - Effective porosity profile of the Berea sample BE-K15B. The average value for the subtracted dataset is 19.3% and for the binarized dataset is 17.3%.

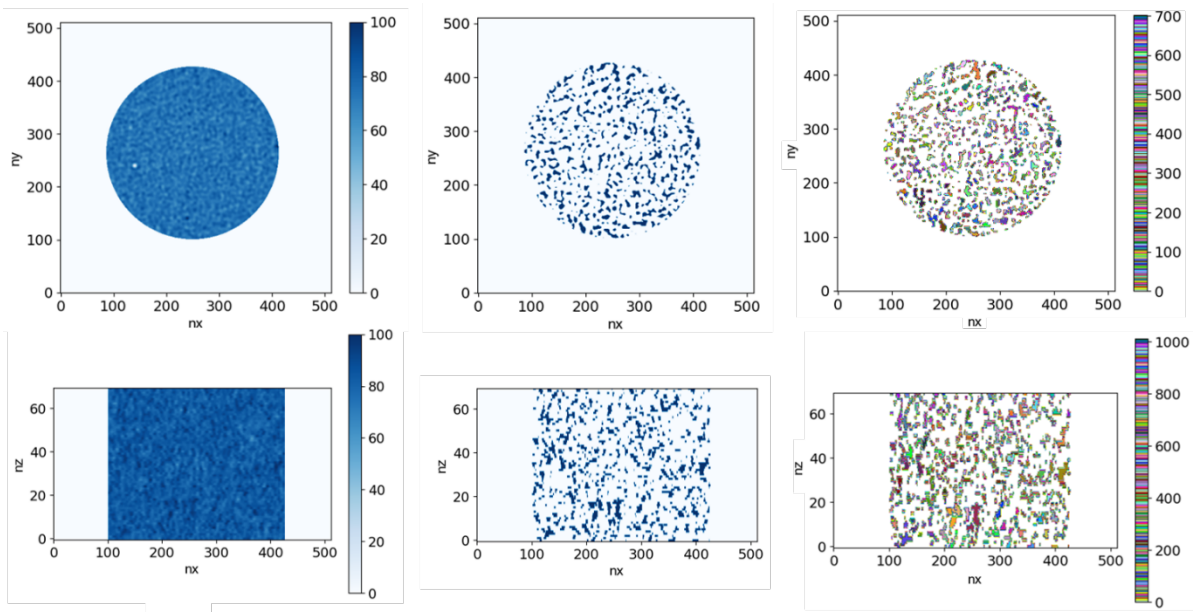


(a) Subtracted data (b) After binarization (c) After Watershed segmentation

Figure 25: Berea sandstone sample - Representation of the effective pore network along slice 41 for the x-y axis and slice 256 for the x-z axis. a) Subtracted data: Blue scale indicates the amount of water (from 0% (white, i.e. a voxel with no pore) to 100% (white, i.e. a voxel completely occupied by a pore), b) after binarization (blue phase : pores, white phase : matrix) using Otsu's method (Otsu, 1979) and (c) after segmentation using the ITK Watershed algorithm to separate macropores.

Application of the ITK Watershed segmentation algorithm to the binarized dataset (Figure 25) indicated that the pore size distribution in the Berea sandstone is very heterogeneous, with most of the population corresponding to small pores (100 voxels and smaller), but also having a significant number of moderately large pores (> 1000 voxels) (see Figure 26). A total of 934 (macro) pores were identified, with a mean pore volume of 1080 voxels (i.e. 6.48 $mm^3$), a median value of 682 voxels (4.01 $mm^3$), a minimum 18 voxels (i.e. 0.11 $mm^3$) and a maximum of 7124 voxels (42.74 $mm^3$). This maximum size is smaller than for the Boise sandstone (73.27 $mm^3$), but this sample shows more small pores, the majority of the population (≈60%) being comprised between 0 and 1000 voxels (against 46% for the Boise sample pore distribution). The fact that the Berea sample is less porous than the Boise sample suggests that the Berea pore network is less well connected with a higher tortuosity. Indeed, the tortuosity analysis (Figure 27) shows an elevated mean tortuosity factor of 11.8 (just over twice the Boise tortuosity value) and indicates a particularly strong anisotropy in the z-direction (tau = 32.1 in the z axis). The differences in porosity and tortuosity between these two sandstones can be explained by differences in grain size, maturity and sphericity, as well as by the distinct cementation style between the grains.

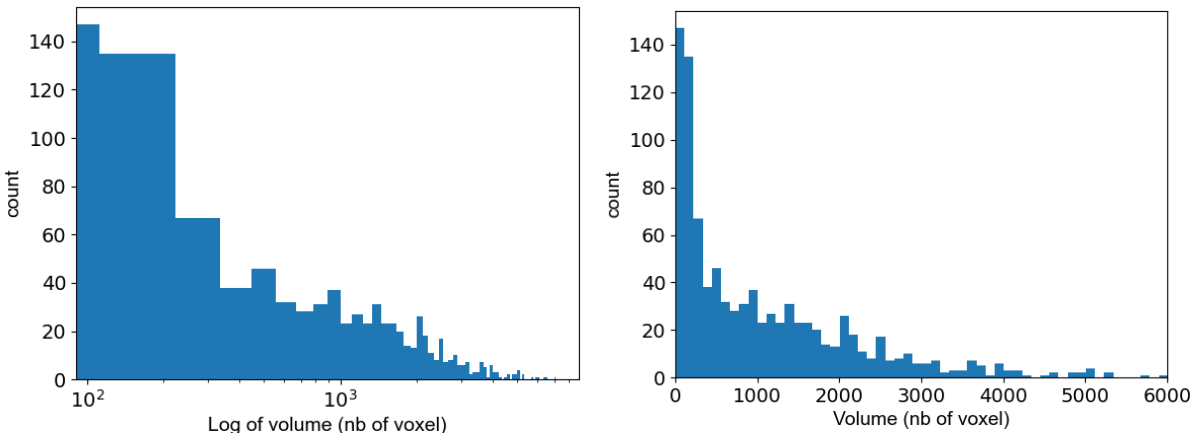


(a) (b)

Figure 26: Berea sandstone sample - Statistical distribution of the (macro) pore size of the Berea sandstone using the ITK Watershed algorithm: a) linear plot best showing the majority of the population b) semi-log plot presenting the entire population.

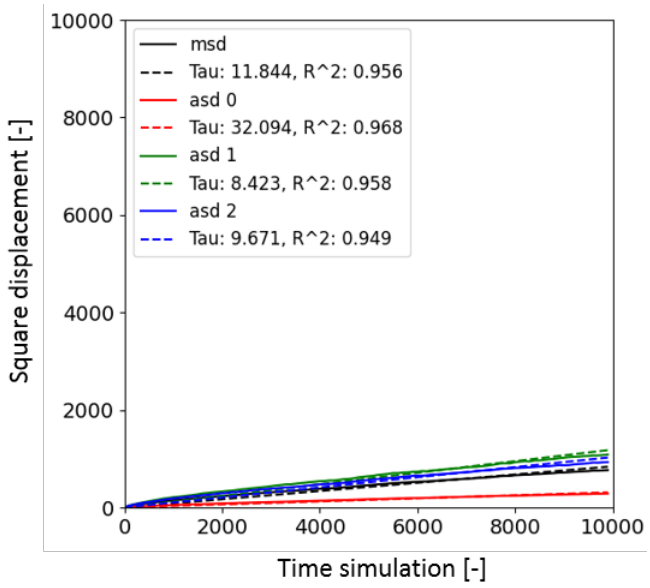


Figure 27: Berea sandstone sample - Mean (MSD) and axial (ASD) square displacement (0: z-axis 1: x-axis 2: y-axis) versus time for the Berea sandstone sample. The plain lines represent the actual results and the dotted lines are the linear regressions for which the slope defines the tortuosity (Tau).

### 5.2.4. Indiana limestone core sample

Based on the work of Larmagnat et al. (2019), the Indiana limestone sample used here (IN-C15A) was found to have an average effective porosity value of 16.2% (Figure 28a). Figure 28 (b-c) also presents a 3D view of the sample and a cross-section resulting from the binarizarion of this med-CT (subtracted) dataset.

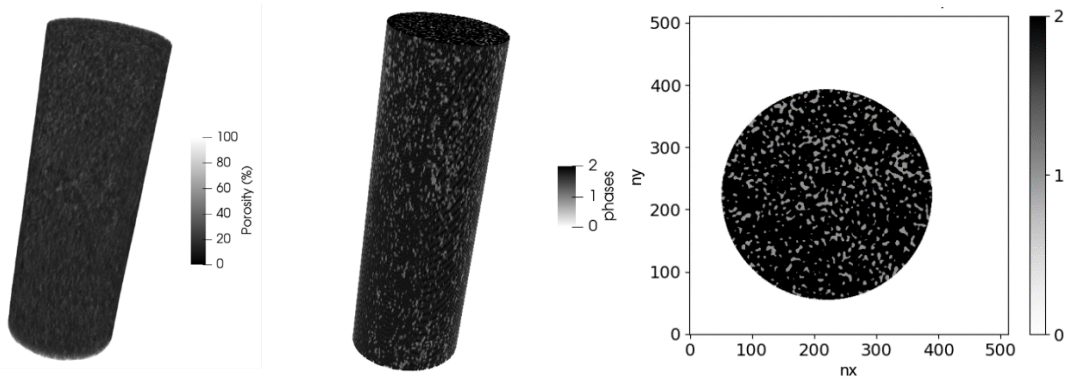


(a) (b) (c)

Figure 28: Indiana limestone sample (IN-C15A) with dimensions [nx,ny,nz]=[512,512,159] and resolution dx=dy=0.1mm and dz=0.6mm. (a) 3D view of the effective porosity dataset estimated using med-CT images from saturated and dry states, from Larmagnat, et al. (2019). The grey scale indicates the amount of water replacing the air space in the sample: from 0% (black, i.e., a voxel completely occupied by the geomaterial) to 100% (white, i.e., a voxel completely occupied by a pore). (b) 3D view illustrating binarized med-CT using Spam and (c) transversal slice through the binarized dataset showing the different phases (in the middle of the sample) – phase 0 (white): outside the media, phase 1 (grey): pores, phase 2 (black): matrix.

Consistent with its lithology, the Indiana limestone contains the smallest pores of the three and thus appears homogeneous to the naked eye. Similarly to the previous two samples, the effective porosity profiles were obtained for both the subtracted and binarized datasets. The binarized dataset (Figure 29, blue line) provide effective porosity values ranging between 10% and 19%, with an average effective porosity for the core sample of 13.5%. For the subtracted dataset, values range between 14.5% and 15.5%, with a mean value of 14.7% (Figure 29, orange line).

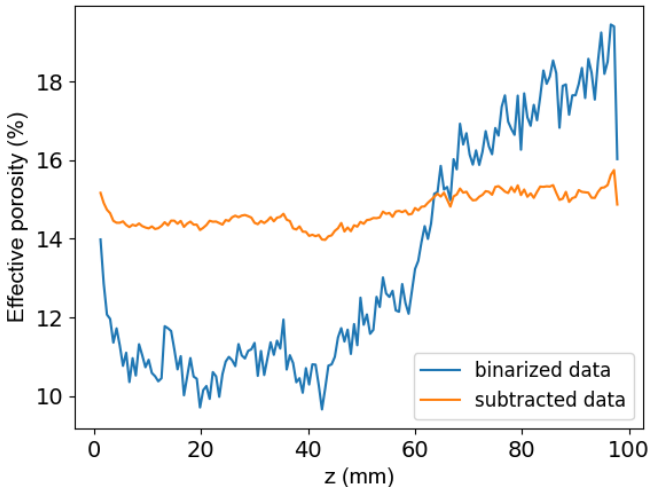


Figure 29: Indiana limestone sample - Effective porosity profile for the Indiana sample IN-C15A. The average value for the subtracted data is 14.7% and for the binarized data is 13.5%.

These two average values are again slightly lower than the mean values obtained from gas porosimetry for a core plug (16.3% see Table 2). Figure 29 also shows that the binarized effective porosity varies locally and increases along the sample length, in contrast with the subtracted dataset, which is relatively constant. Comparison of the subtracted and the binarized datasets, for given longitudinal slices, indicated that the binarization process generates artificial macropores and connections between macropores at some locations or, conversely, neglects microporous areas that are erroneously labeled as rock matrix. A representation of the effective pore network for a given x-y and x-z slice obtained at the different steps during the process is provided in Figure 30.

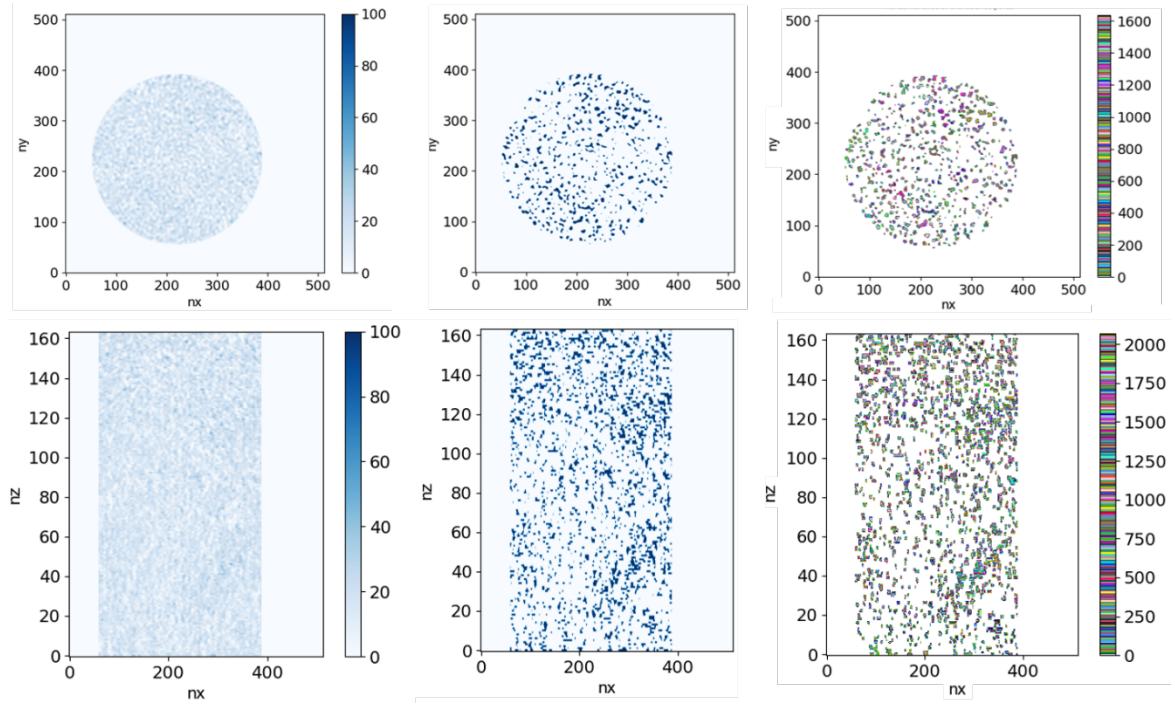


(a) Subtracted data (b) After binarization (c) After Watershed segmentation

Figure 30: Indiana limestone sample - Representation of the effective pore network along slice 79 for the x-y axis and slice 256 for the x-z axis. a) Subtracted data: The blue scale indicates the amount of water (from 0% (white, i.e. a voxel with no pore) to 100% (white, i.e. a voxel completely occupied by a pore), b) after binarization (blue phase : pores, white phase : matrix) using Otsu's method (Otsu, 1979) and (c) after segmentation using the ITK Watershed algorithm to separate macropores.

Applying the ITK Watershed algorithm (Figure 30c) to the binarized dataset (Figure 30b), indicated that most pores measure between 100 and 300 voxels (i.e. 0.6 and 1.8 $mm^3$) (Figure 31a and b). A total of 2 080 (macro) pores were identified. The mean pore volume is 944 voxels (i.e., 5.66 $mm^3$), the median is 270 voxels (1.62 $mm^3$), and the minimum and maximum pore volumes are of 13 voxels (i.e. 0.078 $mm^3$) and 29 894 voxels (179.3 $mm^3$), respectively. Very few medium to large pores (> 2000 voxels) were identified (they only represent 11%). The fact that pores are very small in this material could

explain why this sample shows the largest difference between mean porosity values obtained with the binarized dataset (13.5%) and porosimetry (16.3%) and especially the largest difference between the two ends of the sample (an increase of 10% to 19% from one end to the other). In addition, carbonates are also known to be much more complex porous media than sandstones (e.g., multiple porosity/permeability features), which has a significant impact on pore and pore throat geometries. The binarization likely led to the generation of more artificial pores and connected pathways than in other samples, suggesting that this approach (i.e., using a med-CT scan) is not applicable to this type of fine-grained rock.

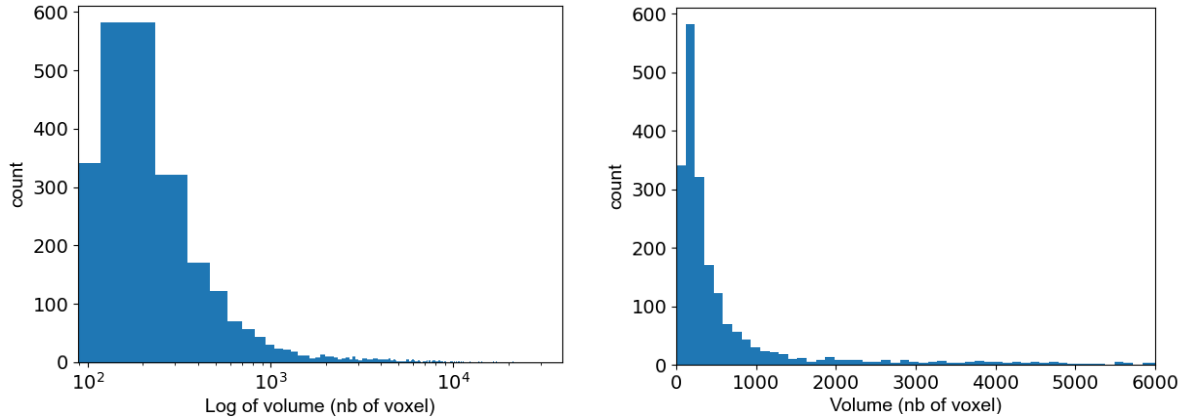


(a) (b)

Figure 31: Indiana limestone sample - Statistical distribution of the (macro) pore size of the Indiana limestone sample using the ITK Watershed algorithm: a) linear plot best showing the majority of the population b) semi-log plot presenting the entire population.

The tortuosity analysis (Figure 32) shows a large mean tortuosity factor of 28 and an extremely strong anisotropy in the z-direction (tau = 136 in the z axis). The high level of tortuosity of the Indiana limestone is likely due to the high dominance of very small pores with very little (if any) connection at this scale (i.e., using the med-CT). Nonetheless, the tortuosity might have been overestimated due to the limitations of the approach, as explained above. To improve the analysis and assessment of the effective porosity in such fine-grained geomaterials, it will be necessary to use micro-CT scan images.

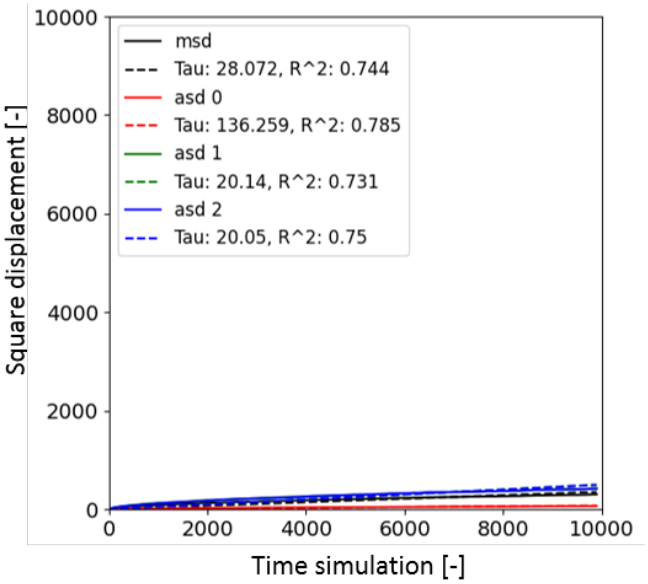


Figure 32: Indiana limestone sample - Mean (MSD) and axial (ASD) square displacement (0: z-axis 1: x-axis 2: y-axis) versus time for the Indiana limestone sample. The plain lines represent the actual results and the dotted lines are the linear regressions for which the slope define the tortuosity (Tau).

## 5.3 Influence of the core sample diameter on the effective porosity evaluation

For an ideal homogeneous material, core size or cross-section orientation would have no influence on the intrinsic parameters. However, in real materials such as rock samples, scanning should ideally be performed using multiple samples and both horizontal and vertical cores to characterize the heterogeneity of the rock unit. In addition, the largest core diameter available should ideally be scanned to include as much heterogeneity as possible in order to obtain representative parameter values, within the limitations associated with the type of CT-scan used. Subtracted and binarized datasets provide the opportunity to explore different numerical sampling strategies, without having to actually cut the rock samples and using relatively low computing time. Moreover, these calculations can also allow comparison of values obtained from different core sizes.

For the three lithologies tested, numerical sampling was performed at three different core diameters: D, 0.75D and 0.5D in order to investigate the sensitivity of the effective porosity assessment considering different rock types. Figure 33 shows that the Boise sandstone, which has the highest value of porosity, also has the lowest standard deviation when using the binarized dataset (0.79%-1.18%) due to its relative homogeneity and the fact that it contains a majority of moderate to large pore size. In contrast, the Indiana limestone, which has the finest grains size and is the least porous lithology, has the highest standard deviation (2.96%-3.11%) value because the vast majority of pores are small (89%

< 2000 voxels) and their size distribution is broad (Figure 35). However, subtracted datasets provide similar values for the three diameters for all three samples.

For the Boise sandstone, the sampling diameter therefore has little effect on the average porosity value for both binarized and non binarized datasets. It remains stable for the three diameters with values ranging from 30.2 to 30.0% with little variation σ≈1.0% for the binarized datasets and from 30.6 to 30.8% with little variation σ≈0.4% for the subtracted datasets. Nonetheless, the standard deviation increases significantly between D and 0.5D (from 0.9 to 1.2% for the binarized datasets and from 0.3 to 0.6% for the subtracted datasets). Interestingly, in highly porous areas, such as when z= 5 and 10 mm (Figure 33), the standard deviation can increase significantly, illustrating that the porosity value will be more impacted by larger pores when a smaller sampling diameter is used, leading to an overestimation of the porosity. A direct comparison between the binarized and subtracted datasets indicates that the mean effective porosities are very similar, nonetheless with nearly twice the standard deviation after the binarization process.

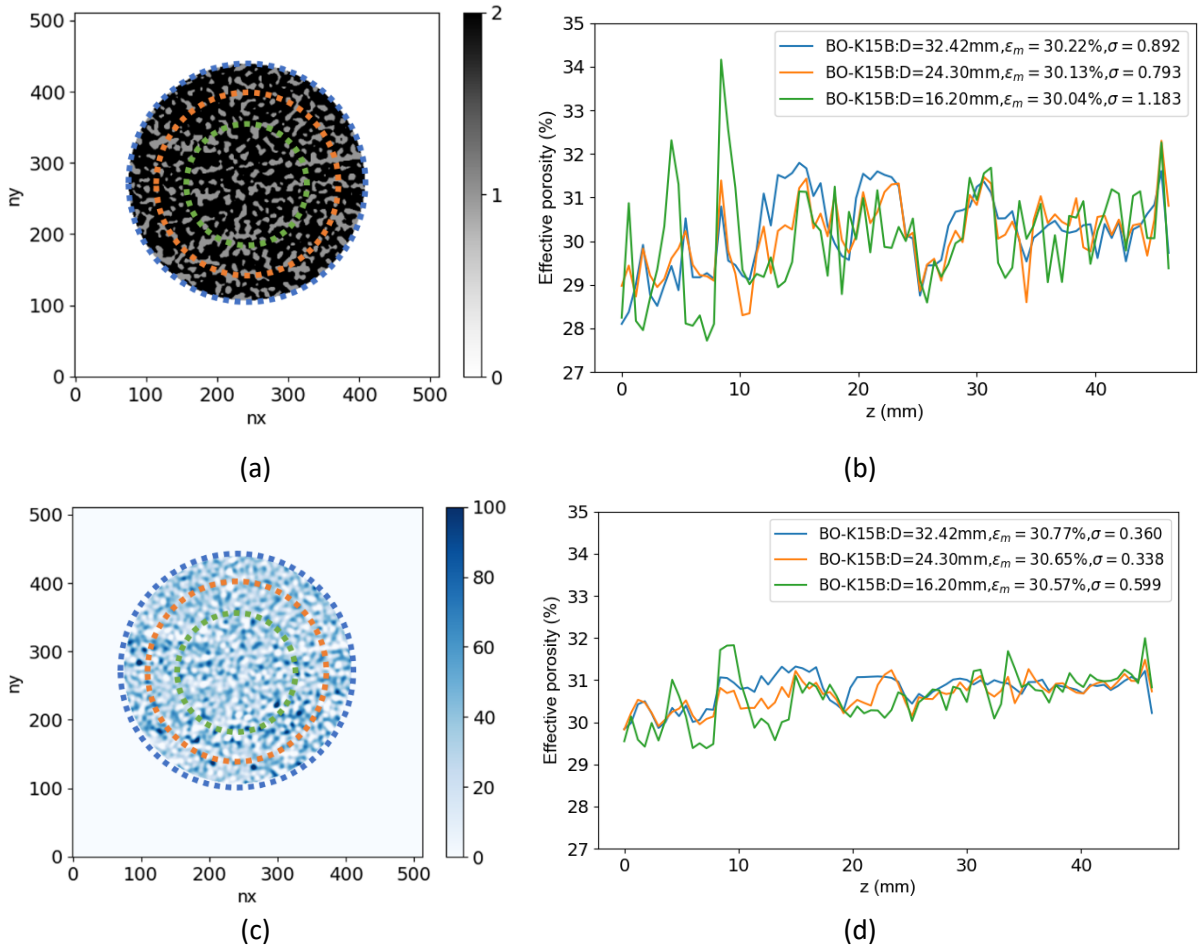


Figure 33: Numerical assessment of the effective porosity according to three diameters within the Boise sandstone sample (D= 32.42 mm (blue line), 24.30 mm (orange line) and 16.20 mm (green line)): (a) cross-section from the binarized dataset and (c) cross-section from the subtracted dataset showing

the different diameters with colors (blue, green and orange). Effective porosity profiles of theses samples: (b) for the binarized datasets and (d) for the subtracted datasets. The average ($\varepsilon_m$) and standard deviation ($\sigma$) effective porosity values are given for each sampling diameter.

For the Berea sandstone, the sample diameter does not significantly affect the average porosity value either; it decreases only slightly from D to 0.5D both for the binarized datasets (from 17.3% to 16.7%) and subtracted datasets (from 19.3% to 19.0%). In terms of variation, the overall standard deviation of the binarized datasets is again typically around 1% and also increases marginally with decreasing diameter, but can locally vary significantly (e.g., around z = 17 mm and = 23 mm) (Figure 34b). The overall standard deviation of the subtracted datasets is lower (around 0.25%) and remains quite stable for all three diameters. It can also locally vary significantly (same example around z = 17 mm and = 23 mm) (Figure 34d). The comparison between binarized and subtracted datasets shows that the different effective porosities are a little more variable than for the Boise sandstone sample and that the binarized datasets provide more variable values for a given profile and larger differences among the three profiles. Therefore, despite the relative homogeneity of the Berea sandstone (usually considered a reference for reservoir studies because of its homogeneity), the sampling diameter could affect the porosity evaluation, especially when using short/small samples, potentially leading to over- or underestimated values, which could locally be very different.

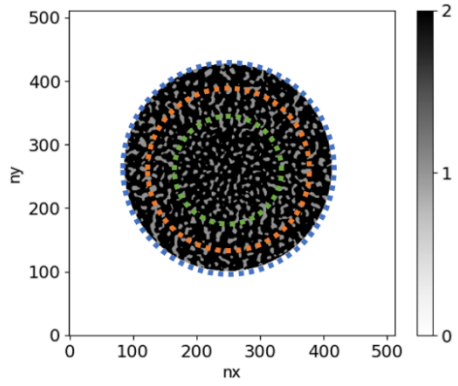


(a)

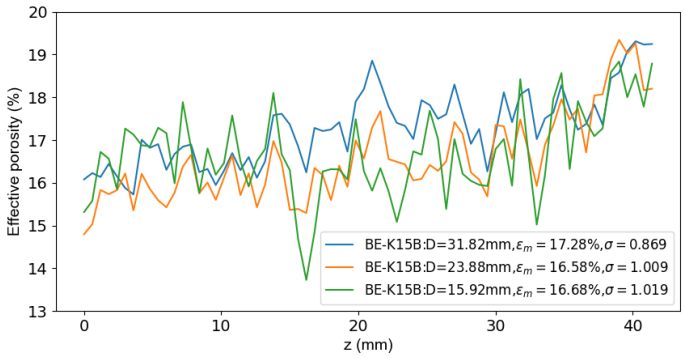


(b)

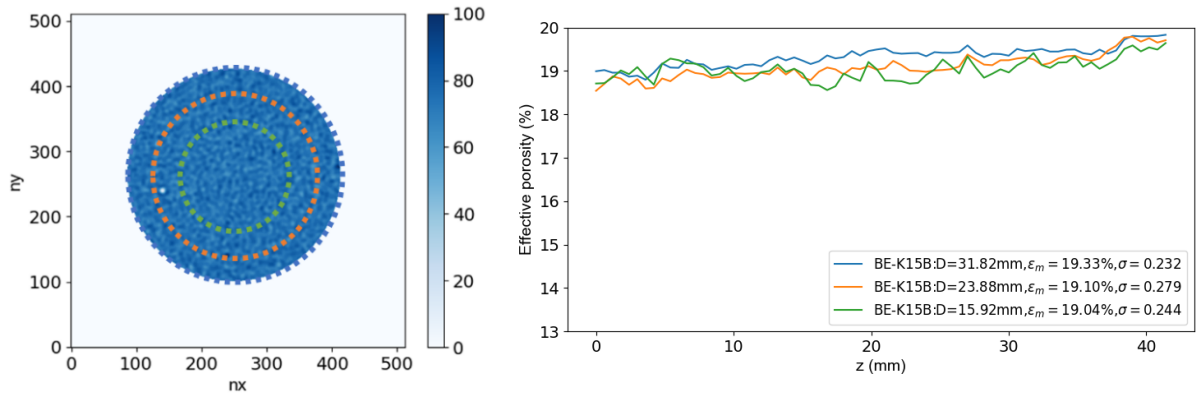


(c) (d)

Figure 34: Numerical assessment of the effective porosity according to three different diameters with the Berea sandstone sample (D= 31.82 mm (blue line), 24.88 mm (orange line) and 15.92 mm (green line)): (a) cross-section from the binarized dataset and (c) cross-section from the subtracted dataset showing the different diameters with colors (blue, green and orange). Effective porosity profiles of theses samples: (b) for the binarized datasets and (d) for the subtracted datasets. The average ($\varepsilon_m$) and standard deviation ($\sigma$) effective porosity values are given for each sampling diameter.

The largest effect of sampling diameter on the average porosity value is observed with the Indiana limestone sample, especially for the binarized datasets, when going from D to 0.5D, where an overall decrease of 1.4 % porosity is obtained on this low porosity material (from 13.5 to 12.1%) (Figure 35b). This material has the lowest porosity and the highest standard deviation by far for the binarized datasets, due to its fine-grained lithology and large pore size distribution, but $\sigma$ values remain quite stable with the sampling diameter (ranging only from 3.0 to 3.1%). The subtracted datasets also show the greatest variation (proportionally to the porosity) and an increase for the smallest diameter (0.5D) compared to the others (0.47% versus 0.40% and 0.38%) (Figure 35b). Therefore, a smaller sampling diameter could likely not account for the contribution of irregular and large pores and induce an underestimation of the average sample porosity.

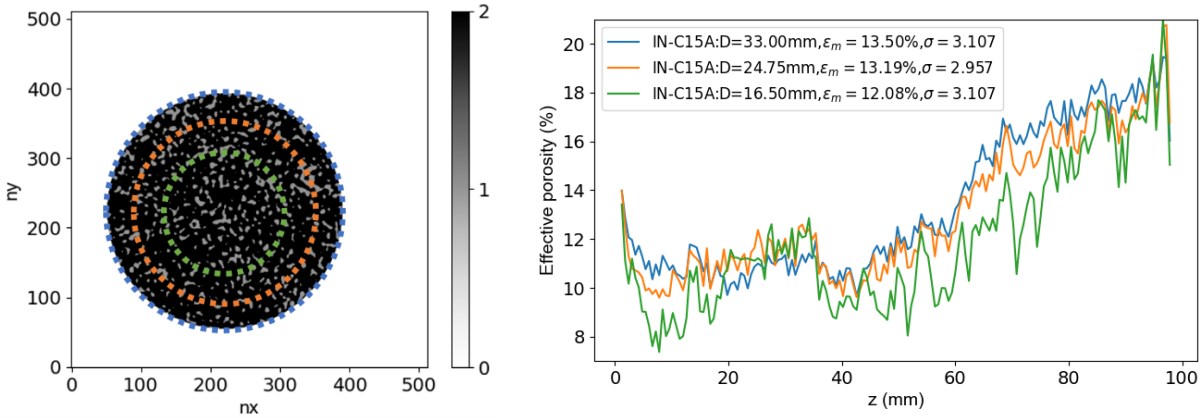


(a) (b)

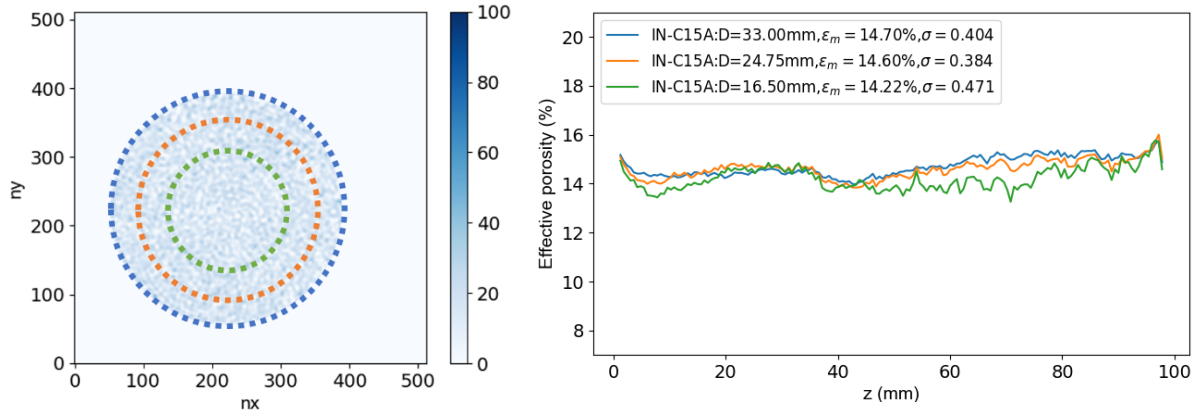


(c) (d)

Figure 35: Numerical assessment of the effective porosity according to three different diameters with the Indiana limestone sample (D= 33.00 mm (blue line), 24.75 mm (orange line) and 16.50 mm (green line)): (a) cross-section from the binarized dataset and (c) cross-section from the subtracted dataset showing the different diameters with colors (blue, green and orange). Effective porosity profiles of theses samples: (b) for the binarized datasets and (d) for the subtracted datasets. The average ($\varepsilon_m$) and standard deviation ($\sigma$) effective porosity values are given for each sampling diameter.

## 5.4 Future work

Our goal being to simulate fluid flow and heat transfer using meshes generated from CT images of geomaterials, the second part of this study will focus on a method first proposed by Roubin et al. (2015) and developed further by Stamati et al. (2018b) for concrete samples, allowing the projection of CT images on an unstructured mesh.

### 5.4.1. Projection of morphologies on an unstructured mesh

Once the two phases (pores and solid matrix) will have been identified satisfactorily using the image processing tools available in Spam (Figure 36a), the morphologies will be projected onto a “void” unstructured mesh of the entire domain (Figure 36b) with a characteristic length defining the spacing between nodes based on the average size of the pore throat. This unstructured 3D mesh will be made of 4-node tetrahedral elements and will be morphology-independant (i.e. with nodes distributed randomly in space). This means that the resulting mesh will not exactly conform to the phase surfaces, but will instead generate a thick boundary between the pores and the solid matrix to allow the integration of certain physical properties (originally to account for the local failure mechanisms[6]).

[6] As the cells (or elements) are "straddling" the interface, this thickens them by construction. Even if the deformation tool is not necessary because there are no discontinuities such as fractures, this function is still necessary to define the normal.

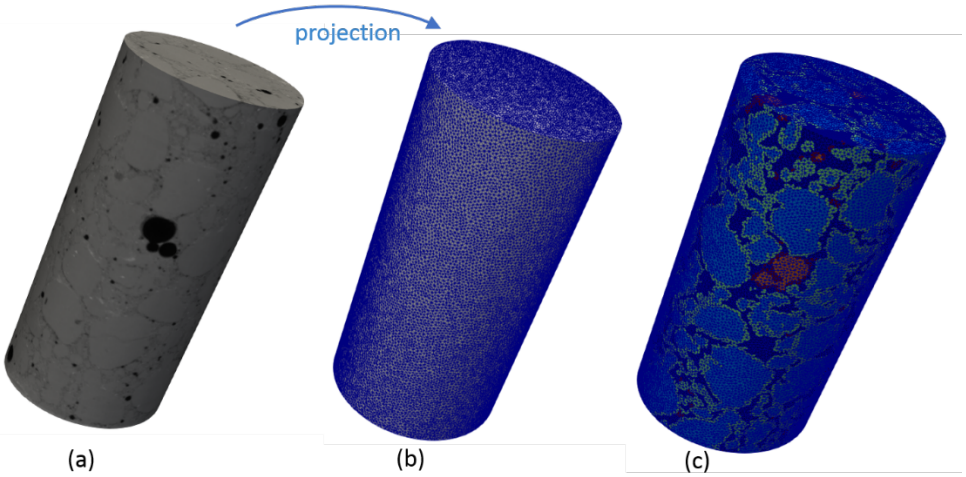


Figure 36: Example of a morphology-independant mesh method for a concrete sample: (a) segmented 3D image (b) a void unstructured mesh (c) the result of this projection: the projected mesh. Adapted from Stamati et al. (2018b).

To project the various phases on a mesh, the first step is to compute a distance field (i.e., spatial fields of scalar distances to a given surface geometry) corresponding to each phase type. Indeed, in grayscale morphology, the images can be transformed into functions, mapping an Euclidean space or grid, and these distance fields are necessary since the computation of the interface vector requires a gradient to calculate an accurate orientation. Thus, these functions are used on each inclusion type phase, then projected on an unstructured mesh. In Spam algorithms, the pore surfaces (Figure 37b) and the normals of pore surfaces (Figure 37c) are generated.

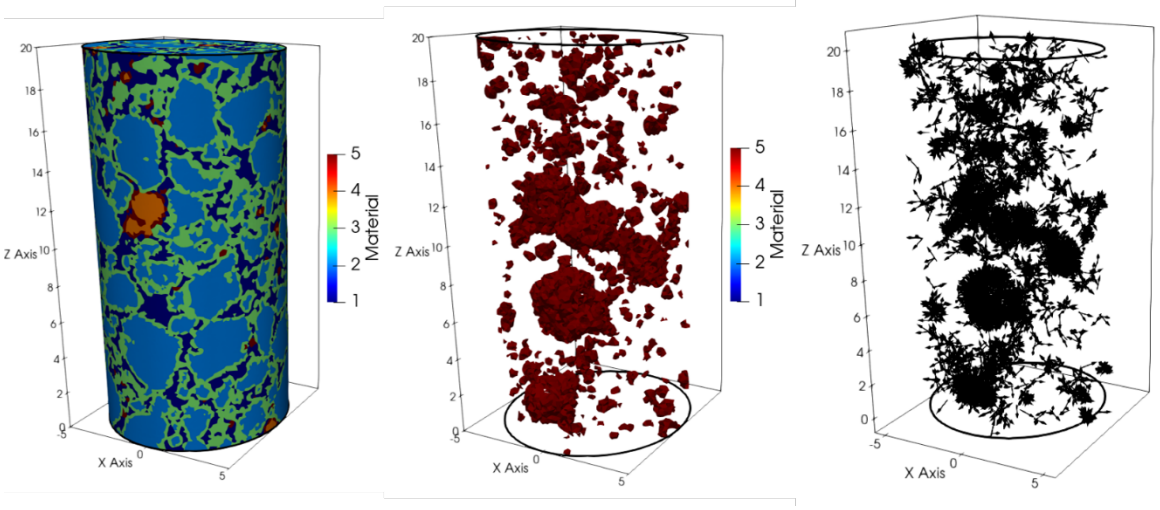


Figure 37: Example of a projection for a concrete sample: (a) Illustration of the projection of each inclusion type phase. Color code: Material 1 (dark blue): mortar, Material 2 (light blue): aggregates, material 3 (green): interface mortar/aggregates, Material 4 (orange): pores and Material 5 (red)

interface mortar/pores. (b) Illustration of pores (Material 4 & 5) (c) representation of the normals of pore surfaces.

Finally, the mesh files generated using Spam will provide a list of coordinates corresponding to the node positions and a list of elements corresponding to the connectivity matrix (corresponding to the numbering of the tetrahedral elements and their arrangement in relation to each other) and the interfaces information.

### 5.4.2. Technical challenges

At this stage of the work, two technical challenges need to be taken into consideration, which will influence the following work:

(i) First, in order to couple a 3D mesh with a CFD software, and in particular a mesh that has information necessary for solving the physics of the problem (such as porosity fields, pore morphologies, etc.), it is necessary to implement an interface that allows communication in the language specific to the chosen software and therefore, that requires technical adjustments according to the choice of the hydrodynamic model and the CFD software. The main benefit of a common exchange format is to reduce the complexity of the code coupling. It also allows sharing such high level functionalities as computation of nodal connectivity of sub-elements (faces and edges), arithmetic operations on fields, entity location functionalities, and interpolation toolkit.

(ii) The second point deals with a specific aspect of numerical analysis and modeling: the resolution of the med-CT, which is 0.1x0.1x0.6mm per voxel for the studied geological samples. Such resolution is not sufficient to generate accurate pore models when most pores are small (< 0.1x0.1x0.6mm). A Silurian dolomitic limestone core sample (CSI-11 from Larmagnat et al. (2019), not detailed in this study), with low porosity and high heterogeneity (Figure 38b&c), illustrates the complexity of setting up a mesh and numerical flow simulations. The Indiana limestone would also present quite a challenge.

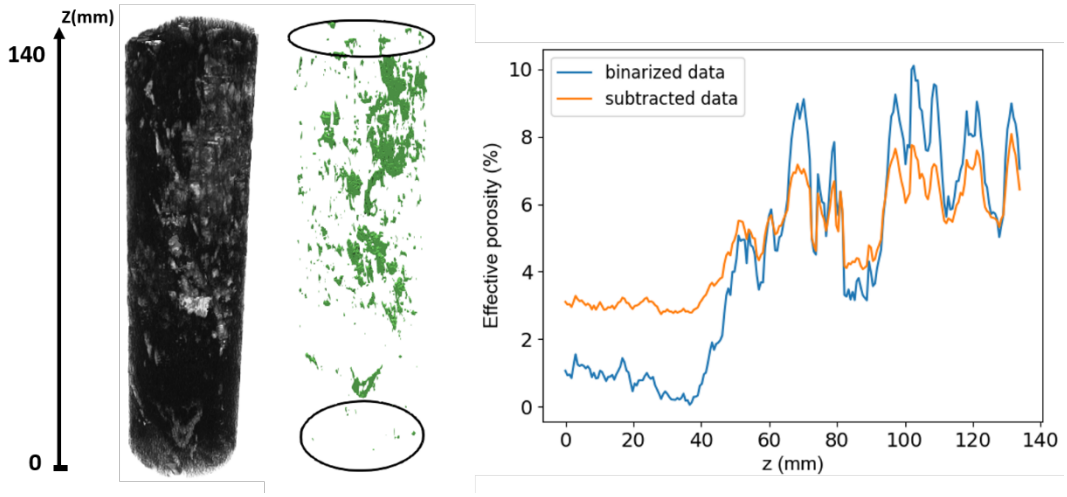


(a) (b) (c)

Figure 38: (a) Example of a 3D view illustrating connected porosity matrices of a Silurian core sample CSI-11 from [Larmagnat et al., 2019]. The grey scale indicates porosity: from 0% (black) to 100% (white). (b) a 3D view of a binarized pore network (c) Effective porosity profile of this sample. The average porosity value for this core plug for the non-binarized data is 4.9% and for the binarized data is 4.4%. Note: over the first 50 mm of the sample, the porosity is lower than in the rest of the sample (around 4.4-4.9%) and includes micro-pores, which are not detectable at the med-CT scale, but play a role in the connectivity of macropores during the saturation experiment. The binarized dataset cannot account for the contribution of micro-pores to the total porosity and therefore leads to underestimates.

These two topics are intrinsically linked to the choice of the hydrodynamic model that we will use in the second part of this study.

### 5.4.3 Perspectives: Toward a CFD Coupling

To assess the permeability of a porous material, numerical modeling is a relevant choice when reliable and accurate tools are available and also, when the uncertainty (i.e., the margin of error from the measurements) of the data (e.g. CT-scanning) can be determined and compared with the property magnitude. However at this step of the work, the estimation of cumulative errors is unknown and will have to be determined. One way to accomplish this task is to have reference solutions (analytical or experimental) that allow the measurement of the uncertainty associated with the numerical solution. There are at least two ways to have a reference solution in this case: conduct a lab experiment and obtain high resolution porosity network data from a micro-CT scan. For the second step of this upcoming study, the second option was adopted. A multiscale approach (Figure 39) allows for overlaps between scales and, in a cascading sequence, the comparision of a given coarse scale mesh with another mesh at a finer scale (i.e., from the reference solution). In the present section, we provide some guidelines to develop our future framework for our mesoscale modeling that would meet the needs of geothermal energy modeling applied to the Becancour area.

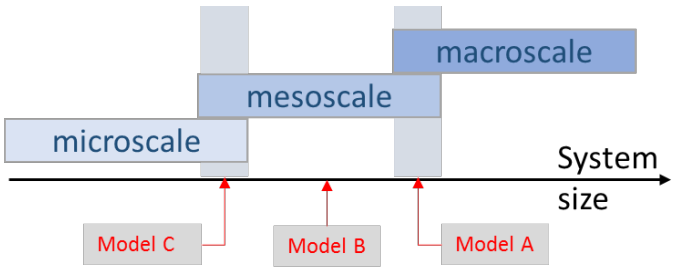


Figure 39: Illustration of the multi-scale approach to be used in support to geothermal energy modeling

For a meso-model, the Navier-Stokes equations (1)-(2) need to be modified to close the physical problem. Thus, an alternative formulation taking into account the resistance of the porous medium can be used, by introducing a source term in equation (1):

$$\boldsymbol{F} = -\left(\frac{\mu}{k}\boldsymbol{u} + \rho\frac{C}{2}|\,\boldsymbol{u}|\,\boldsymbol{u}\right) \tag{9}$$

For instance, the permeability k and the inertial loss coefficient C can be modeled from the equation provided in Ergun (1952) (equation 8) as :

$$k = \frac{1}{\alpha}\,\frac{\epsilon^3}{(1-\epsilon)^2\Sigma^2} \;\; and \; C = 2\beta\,\frac{(1-\epsilon)\,\Sigma}{\epsilon^3} \tag{10}$$

The use of different resolutions for mathematical models is possible for this scale. The meso-model A (illustrated in Figure 39) is close to a macro-scale approach, where no micro heterogeneity of the porosity can be taken into account. The meso-model B (see Figure 39) is a model where the local porosity per slice provided by CT-scan data can be used, corresponding to the volumetric average of void fraction of a sample slice of thickness *dz*. A possible improvement for very heterogeneous samples would be to use a projected mesh presented in the section 5.4.1. First, a two-phase mesh (i.e.,the matrix and pore space are considered separately, using a fluid phase and a solid phase) will be developed. However, the major limitation of this approach is that the network of connected pores may not be fully captured. Finally the meso-model C (see Figure 39) is a model integrating a multiphase formulation of the flow that makes it possible to compute the velocity and pressure fields transformed by the porosity field in each computational cell as follows:

$$\frac{\partial\epsilon\rho\boldsymbol{u}}{\partial t} + \nabla\cdot(\epsilon\rho\boldsymbol{u}\boldsymbol{u}) = \boldsymbol{\nabla}\cdot(\epsilon\boldsymbol{\tau}) - \epsilon\boldsymbol{\nabla}p - \left(\frac{\mu}{k}\boldsymbol{u} + \rho\frac{C}{2}|\,\boldsymbol{u}|\,\boldsymbol{u}\right) \tag{11}$$

$$\frac{\partial\epsilon\rho}{\partial t} + \nabla\cdot(\epsilon\rho\boldsymbol{u}) = \boldsymbol{0} \tag{12}$$

The meso model A is often used in commercial software (ANSYS, COMSOL, etc.), employing a user-defined function. This model does not necessarily need medical CT-scan datasets, but could be used for comparison. Models B and C are more appropriate for our objectives, and will be compared in a second step of this work.

It is also planned to compare the numerical results with those of a laboratory-scale model using the entire core sample, through which a known fluid flow and heat flux will be imposed. Several sensors distributed throughout this model will help validate the numerical models.

# 6. Conclusion and perspectives

The first phase of this study resulted in three main achievements. First, building on previous work where an approach was developed on a quasi-ideal porous media composed of glass beads, pre-existing medical CT-scan datasets of reference materials with varied lithologies (Indiana limestone, Berea and Boise sandstone cores) were used to extract a 3D geometry of connected pore networks using the open-source software Spam. Second, new results were generated using both subtracted and binarized datasets that provided effective porosity profiles along the cores. Then segmentation allowed the assessment of pore size distributions and sample tortuosity. These estimates were proposed as a tool to discriminate which lithology and image resolution might be appropriate to run realistic flow and heat transfer simulations using med CT-scan images. Third, an approach for future fluid flow simulations into these connected pore networks was presented, considering the limitations of the med-CT images. The image resolution relative to the pore size is critical to build realisic pore networks that can be subsequently used to investigate fluid flow and heat transfer for geothermal energy purposes. Based on our results, the Boise sandstone dataset can be used with both a two-phase and multiphase model, while the Berea sandstone and the Indiana limestone current datasets (obtained from med-CT scan images) will not be retained for the use of a two-phase model in the second part of the study. However, micro-CT image acquisition would probably allow the use of just about any sample, as long as the computing power is available.

The perspective for the second phase of the work is to transfer the 3D geometry of a glass bead medium into a 3D two-phase model for incompressible fluid flow and heat transfer simulations and compare the results with those from literature. Then, acquire micro CT images of the Boise sandstone sample (and of other samples if time allows, in particular the reference Gambier limestone which has much coarser grains than the Indiana limestone), to provide 3D images of the porosity network at a smaller scale. The Boise sandstone and Gambier limestone appear promising, based on the binarized

/subtracted comparison. Finally, for these two lithologies, a comparison will be made between the results obtained with images from medical CT and micro-CT. From these could result adjustments of the 3D models generated with the medical CT datasets and an improved methodology.

# 7. References


Aharonov, E., M. Spiegelman, and P. Kelemen, 1997, Three‐dimensional flow and reaction in porous media: Implications for the Earth's mantle and sedimentary basins: Journal of Geophysical Research: Solid Earth, v. 102, p. 14821-14833.

Andrä, H., N. Combaret, J. Dvorkin, E. Glatt, J. Han, M. Kabel, Y. Keehm, F. Krzikalla, M. Lee, and C. Madonna, 2013a, Digital rock physics benchmarks—Part I: Imaging and segmentation: Computers & Geosciences, v. 50, p. 25-32.

Andrä, H., N. Combaret, J. Dvorkin, E. Glatt, J. Han, M. Kabel, Y. Keehm, F. Krzikalla, M. Lee, and C. Madonna, 2013b, Digital rock physics benchmarks—Part II: Computing effective properties: Computers & Geosciences, v. 50, p. 33-43.

API, 1998, RP40, Recommended practices for core analysis, 2nd Ed., Washington, DC, American Petroleum Institute.

Archie, G. E., 1952, Classification of carbonate reservoir rocks and petrophysical considerations: Aapg Bulletin, v. 36, p. 278-298.

Bear, J., 2018, Modeling phenomena of flow and transport in porous media, v. 1, Springer.

Beare, R., and G. Lehmann, 2006, The watershed transform in ITK - discussion and new developments, Monash University, p. 17.

Burke, S., and W. Plummer, 1928, Suspension of Macroscopic Particles in a Turbulent Gas Stream1: Industrial & Engineering Chemistry, v. 20, p. 1200-1204.

Cantrell, D. L., and R. M. Hagerty, 1999, Microporosity in Arab Formation Carbonates, Saudi Arabia: GeoArabia, v. 4, p. 129-154.

Carman, P., 1937, Fluid Flow Through Granular Beds Transactions of the Institution of Chemical Engineers, vol. 15.

Carman, P. C., 1956, Flow of gases through porous media.

Chapman, R. E., 1987, Fluid flow in sedimentary basins: a geologist's perspective: Geological Society, London, Special Publications, v. 34, p. 3-18.

Choquette, P. W., and L. C. Pray, 1970, Geologic nomenclature and classification of porosity in sedimentary carbonates: AAPG bulletin, v. 54, p. 207-250.

Churcher, P., P. French, J. Shaw, and L. Schramm, 1991, Rock properties of Berea sandstone, Baker dolomite, and Indiana limestone: SPE International Symposium on Oilfield Chemistry.

Darcy, H., 1856, Les fontaines publiques de la ville de Dijon exposition et application... par Henry Darcy, Victor Dalmont.

Dorai, F., 2015, Étude numérique des chargements et de l'hydrodynamique dans des réacteurs pilotes à lits fixes.

Ergun, S., 1952, Fluid flow through packed columns: Chemical Engineering Progress, v. 48, p. 89-94.

Freire-Gormaly, M., J. S. Ellis, H. L. MacLean, and A. Bazylak, 2016, Pore structure characterization of Indiana limestone and pink dolomite from pore network reconstructions: Oil & Gas Science and Technology–Revue d'IFP Energies nouvelles, v. 71, p. 33.

Fu, J., H. R. Thomas, and C. Li, 2021, Tortuosity of porous media: Image analysis and physical simulation: Earth-Science Reviews, v. 212, p. 103439.

Hammouti, A., F. Oukaili, and D. Pham Van Bang, in preparation, CFD investigation in a Porous Media generated from Computed Tomography Scan: Computers and Geosciences.

Kozeny, J., 1927, Uber kapillare leitung der wasser in boden: Royal Academy of Science, Vienna, Proc. Class I, v. 136, p. 271-306.

Kutsovsky, Y., L. Scriven, H. Davis, and B. Hammer, 1996, NMR imaging of velocity profiles and velocity distributions in bead packs: Physics of Fluids, v. 8, p. 863-871.

Larmagnat, S., M. Des Roches, L.-F. Daigle, P. Francus, D. Lavoie, J. Raymond, M. Malo, and A. Aubiès-Trouilh, 2019, Continuous porosity characterization: Metric-scale intervals in heterogeneous sedimentary rocks using medical CT-scanner: Marine and Petroleum Geology, v. 109, p. 361-380.

Lucia, F. J., C. Kerans, and J. W. Jennings, 2003, Carbonate reservoir characterization: Journal of Petroleum Technology, v. 55, p. 70-72.

McDowell‐Boyer, L. M., J. R. Hunt, and N. Sitar, 1986, Particle transport through porous media: Water resources research, v. 22, p. 1901-1921.

Meyer, F., 1994, Topographic distance and watershed lines: Signal processing, v. 38, p. 113-125.

Neglia, S., 1979, Migration of fluids in sedimentary basins: AAPG Bulletin, v. 63, p. 573-597.

Noiriel, C., and C. Soulaine, 2021, Pore-Scale Imaging and Modelling of Reactive Flow in Evolving Porous Media: Tracking the Dynamics of the Fluid–Rock Interface: Transport in Porous Media, v. 140, p. 181-213.

Otsu, N., 1979, A threshold selection method from gray-level histograms: IEEE transactions on systems, man, and cybernetics, v. 9, p. 62-66.

Oukaili, F., 2019, Réhabilitation des sols contaminés par injection de fluides : comparaison directe entre experimentation CT-Scan et simulation numérique (CFD-DNS), INRS Internship report, p. 41.

Patel, H., J. Kuipers, and E. Peters, 2019, Effect of flow and fluid properties on the mobility of multiphase flows through porous media: Chemical Engineering Science, v. 193, p. 243-254.

Pittman, E. D., 1971, Microporosity in carbonate rocks: AAPG Bulletin, v. 55, p. 1873-1878.

Rakotonirina, A., 2016, Fluid-solid interaction in a non-convex granular media : application to rotating drums and packed bed reactors, Université de Lyon, 176 p.

Rakotonirina, A. D., R. Matthieu, H. Abdelkader, and W. Anthony, under review, Flow through a packed bed of trilobe/quadrilobe particles: non-boundary fitted particle-resolved simulations and pressure drop uncertainty quantification: Chemical Engineering Science.

Ramsey, M., 2019, Schlumberger oilfield glossary: Schlumberger.

Roubin, E., A. Vallade, N. Benkemoun, and J.-B. Colliat, 2015, Multi-scale failure of heterogeneous materials: A double kinematics enhancement for Embedded Finite Element Method: International Journal of Solids and Structures, v. 52, p. 180-196.

Schlumberger, 1989, Log Interpretation: Principles and Applications., Texas, Schlumberger Educational Services.

Stamati, O., E. Andò, E. Roubin, R. Cailletaud, M. Wiebicke, G. Pinzon, C. Couture, R. Hurley, R. Caulk, and D. Caillerie, 2020, Spam: software for practical analysis of materials: Journal of Open Source Software, v. 5, p. 2286.

Stamati, O., E. Roubin, E. Andò, and Y. Malecot, 2018a, Phase segmentation of concrete x-ray tomographic images at meso-scale: Validation with neutron tomography: Cement and Concrete Composites, v. 88, p. 8-16.

Stamati, O., E. Roubin, E. Andò, and Y. Malecot, 2018b, Tensile failure of micro-concrete: from mechanical tests to FE meso-model with the help of X-ray tomography: Meccanica, v. 54, p. 707-722.

Steefel, C. I., L. E. Beckingham, and G. Landrot, 2015, Micro-continuum approaches for modeling pore-scale geochemical processes: Reviews in Mineralogy and Geochemistry, v. 80, p. 217-246.

Tranter, T. G., M. D. Kok, M. Lam, and J. Gostick, 2019, pytrax: A simple and efficient random walk implementation for calculating the directional tortuosity of images: SoftwareX, v. 10, p. 100277.

Ward, J. C., 1964, Turbulent Flow in Porous Media: Journal of the Hydraulics Division, v. 90, p. 1-12.

Yang, K., M. Li, N. N. A. Ling, E. F. May, P. R. J. Connolly, L. Esteban, M. B. Clennell, M. Mahmoud, A. El-Husseiny, A. R. Adebayo, M. M. Elsayed, and M. L. Johns, 2019, Quantitative Tortuosity Measurements of Carbonate Rocks Using Pulsed Field Gradient NMR: Transport in Porous Media, v. 130, p. 847-865.

Yokoyama, T., and S. Takeuchi, 2009, Porosimetry of vesicular volcanic products by a water‐expulsion method and the relationship of pore characteristics to permeability: Journal of Geophysical Research: Solid Earth, v. 114.